Holocene water balance variations in Great Salt Lake, Utah: application of GDGT indices and the ACE salinity proxy

Rachel T. So[1*], Tim K. Lowenstein[2], Elliot Jagniecki[3], Jessica E. Tierney[4], and Sarah J. Feakins[1]

[1]Department of Earth Sciences, University of Southern California, Los Angeles, CA 90089, USA.

[2]Department of Geological Sciences and Environmental Studies, Binghamton University, Binghamton, NY 13902, USA.

[3]Utah Geological Survey, Salt Lake City, UT 84114, USA.

[4]Department of Geoscience, University of Arizona, Tucson, AZ 85721, USA.

Corresponding author: Rachel T. So (rtso@usc.edu)

Key Points:

- Glycerol dialkyl glycerol tetraethers produced by bacteria and archaea detect Holocene limnological changes at Great Salt Lake.
- The Archaeol and Caldarchaeol Ecometric salinity index remains near its upper limit in Great Salt Lake from 7.2 ka to present.
- A 5.5 ka step shift in microbial lipids suggests limnological change coeval with the end of a regional dry spell in the mid-Holocene.

Abstract

Great Salt Lake, Utah, is a hypersaline terminal lake in the Great Basin, and the remnant of the late glacial Lake Bonneville. Holocene hydroclimate variations cannot be interpreted from the shoreline record, but instead can be investigated by proxies archived in the sediments. GLAD1-GSL00-1B was cored in 2000 and recently dated by radiocarbon for the Holocene section with the top 11 m representing ~7 ka to present. Sediment samples every 30 cm (~220 years) were studied for the full suite of microbial membrane lipids, including those responsive to temperature and salinity. The Archaeol and Caldarchaeol Ecometric (ACE) index detects the increase in lipids of halophilic archaea, relative to generalists, as salinity increases. We find Holocene ACE values ranged from 81-98, which suggests persistent hypersalinity with <50 g/L variability across 7.2 ka. The temperature proxy, MBT'_{5Me}, yields values similar to modern mean annual air temperature for months above freezing (MAF = 15.7°C) over the last 5.5 ka. Several GDGT metrics show a step shift in microbial communities and limnology at 5.5 ka. Extended archaeol detects elevated salinity during the regional mid-Holocene drought, not readily detected in the ACE record that is often near the upper limit of the index. We infer that the mid-Holocene GSL was shallower and saltier than the late Holocene. The current drying may be returning the lake to conditions not seen since the mid-Holocene.

Keywords: GDGT, ACE, Holocene, Great Salt Lake

Plain Language Summary

Great Salt Lake in Utah is the remnant of a once much larger lake and is currently at a historically low level. We study a lake sediment core, collected in 2000 from the floor of Great Salt Lake, and recently dated. We take new samples from the core and measure them for molecules made by microbes, whether living in the lake or washed in from the surrounding soils. We reconstruct lake conditions during the last 7,200 years and assess whether lake level fluctuated during that time. Over the past 7,200 years, we find evidence that the lake was shallower from 7,200 to 5,500 years ago but has been relatively stable until the modifications of the lake in the 20th century and the current drying trend.

1. Introduction

Paleoclimate reconstructions of the Holocene provide insights into the stability or sensitivity of our present climate state. While it is a time of relative climatic stability compared to the glacial-interglacial cycles that preceded it, the changes may in some cases be profound especially in zones prone to drought-stress. In southwestern North America, lake sediments and speleothems record a generally wet early Holocene (11 to 8 ka), and a dry middle Holocene (8 to 4 ka) with a return to relatively moist late Holocene (Lachniet et al., 2020 and references therein). Although many Holocene climate modeling studies have struggled to simulate the mid-Holocene warmth, recent modeling has found this emerges with the addition of vegetation feedbacks (Thompson et al., 2022). As the mid-Holocene warming may be an analog for the current warming, it is studied here as context for the current drought in the region.

Great Salt Lake (GSL), UT, USA, at 41.1°N is a remnant of a larger lake, Lake Bonneville. Lake Bonneville reached its maximum size during the termination of the Last Glacial Maximum (LGM) at ~18 ka then shrank to the areal extent of modern GSL by ~13 ka (Oviatt et al., 2021). The drying between the LGM and Holocene greatly increased salinity in the residual lake and left behind the Bonneville salt flats. This drastic shrinking and lake level drop was recorded in preserved shorelines (Oviatt et al., 2021). In contrast, any recessional shorelines of the mid-Holocene arid interval have been lost to subsequent late Holocene transgressions. Instead, continuous geochemical records from sediment cores have potential to reconstruct Holocene climate. As its name implies, Great Salt Lake is salty with current salinity of 120-180 g/L (data for 2010-2021; Rupke and McDonald, 2012), making it hypersaline (>50 g/L salinity). In a closed-basin lake like GSL, salinity is controlled by the hydrologic balance between input from rivers, springs/groundwater, and precipitation, and output as evaporation, with increased evaporation resulting in lower lake levels and higher salinity. Using organic geochemical evidence, we seek to reconstruct GSL salinity and limnological conditions across the Holocene to provide longer context for present-day drying trends and declining lake levels (Wurtsbaugh et al., 2017).

Archaeol is a diphytanyl glycerol diether (DGD), a membrane lipid made by a diverse range of archaea (e.g. Vandier et al., 2021 and references therein) including abundant production by halophilic *Euryarchaeota* (Dawson et al., 2012; Macalady et al., 2004; Teixidor et al., 1993). Proportional abundances of archaeol have been used to track the contrasting salinity of

hypersaline, marine, estuarine, and freshwater environments (Turich and Freeman, 2011). Application of this method to lake sediment cores has revealed large salinity fluctuations in the late Pleistocene in Lake Elsinore (CA) and Searles Lake (CA) (Feakins et al., 2019; Peaple et al., 2022), but the response to more subtle variations in the Holocene has not yet been tested. Another DGD, extended archaeol, has been identified as a more diagnostic biomarker for halolophilic *Euryarchaeota* (Bale et al., 2019; Vandier et al., 2021), but not yet reported from southwestern North American hypersaline lakes.

Aside from DGDs, archaea also produce a number of isoprenoid glycerol dialkyl glycerol tetraethers (isoGDGTs) and these have been used as microbial and environmental indicators in aquatic environments. GDGT-0 (previously referred to as caldarchaeol) is produced by *Crenarchaeota*, *Thaumarchaeota*, and some *Euryarchaeota* (Schouten et al., 2013). High proportions of this compound, in the absence of abundant crenarchaeol, have been used to denote production by methanogenic *Euryarchaeota*, which can be indicative of stratified waters (Baxter et al., 2021; Blaga et al., 2009; Naeher et al., 2014). In stably stratified hypersaline lakes, mixing may occur during lake freshening events (Peaple et al., 2022) or in lakes shallow enough for wind mixing (Stefanescu et al., 2021).

Branched GDGTs (brGDGTs) are bacterial membrane lipids that have also been widely applied to reconstruct paleoenvironments including applications to soils and lacustrine sediments for temperature reconstructions (e.g. Martinez-Sosa et al., 2021; Peterse et al., 2012; Weijers et al., 2007). Complications with lake depth have been noted with this paleothermometry technique in nearby alpine lakes with temperature stratification (Stefanescu et al., 2021). As GSL is located at mid-elevation (1,280 masl) and has density primarily controlled by salinity (rather than temperature), those alpine lake depth complications are not expected to apply. However, the hypersaline environment of GSL may carry additional complications, as salinity outliers have been noted in existing calibrations (Martinez-Sosa et al., 2021). Here, using DGDs, isoGDGTs, and brGDGTs, we generate a 7.2 ka hydroclimate history of GSL to track climate change and limnological conditions from the middle to late Holocene, paying particular attention to the limitations of GDGT proxies in this extreme environment.

1.1. Study location

GSL is a hypersaline terminal lake located in the eastern part of the United States' Great Basin (**Figure 1**). At the lake's historic mean elevation of 1,280 masl (m above sea level), the lake is more than 10 m deep across the central part of the basin and averages 5.5 m deep (Belovsky et al., 2011; Shope and Angeroth, 2015). In 2000, the Global Lakes Drilling (GLAD) initiative drilled four sites to a total of 120 m below lake floor reaching back to the boundary of oxygen isotope stages 6 and 7 (~175 ka) (Dinter et al., 2000). The original study reported density, magnetic susceptibility, minerology, inorganic carbon, and organic carbon from the recovered cores (Dinter et al., 2000). Recently the Holocene sedimentary section in the upper 11 m of GLAD1-GSL00-1B (41.094°N, 112.365°W, 8.4 m water depth) was dated using radiocarbon (Bowen et al., 2019). The Holocene sedimentary sequence is the target for the biomarker reconstructions here.

The modern lake water balance of Great Salt Lake includes inflow from rivers (66%), precipitation (31%), and groundwater (3%) (Jones et al., 2009). The water leaves by evaporation from the closed basin (Jones et al., 2009), although recent work revises groundwater inflow up to 10-12% (Bunce et al., 2022). Instrumental records from 1966 to present indicate 7 m of fluctuation in lake levels (Rupke and McDonald, 2012; United States Geological Survey, 2022b) due to the changing water balance. During the high stand of the last glacial maximum/Heinrich Stadial 1 (HS1), GSL occupied a much greater areal extent, up to ~52,000 km^2, forming freshwater Lake Bonneville (Baxter et al., 2005; Oviatt et al., 2021). Continued downcutting at the outflow point eventually caused rapid overflow during the Bonneville flood, dropping lake levels by 100 m (Oviatt et al., 2021). Since then, the drier climate caused continued lake shrinkage to modern levels by the start of the Holocene, leading to the formation of the Bonneville Salt Flats (west of the present-day GSL) and a reduction of lake size to <10% of its former extent.

Riverine inflow to GSL primarily comes from the Bear (32.5 ± 34.4 m^3/s), Jordan (3.5 ± 1.2 m^3/s), and Weber Rivers (8.1 ± 15.9 m^3/s; all reported as 2000-2020 annual mean discharge). The Bear River records low discharge (2-5 m^3/s) in the dry summer months from July to September, with flow rising consistently during the fall to a plateau of 20-50 m^3/s in January and February. Peak flows occur in March to April, reaching >50 m^3/s, and then drops back down to 2-5 m^3/s by June (United States Geological Survey, 2022a).

The modern GSL is separated into a northern and southern section by a railroad causeway built in 1959. As rivers exclusively flow into the South Arm, salinities are 120-180 g/L, whereas the North Arm has salinities of 290-340 g/L and a permanent halite bottom crust (data for 2010-2021; Jagniecki et al., 2021; Rupke and McDonald, 2012). Salinity is heterogeneous around the shallow lake margins with freshwater influence near river inflows during peak discharge associated with times of snowmelt and evaporative enrichment along other margins, especially during summer and drought. At times in the instrumental record, a halocline has developed in the south arm, with higher salinities at depth and fresher conditions at the surface, but it is currently well mixed (Rupke and McDonald, 2012). While the North Arm is a restricted evaporation pond, the South Arm has major river inflow and is more representative of the pre-causeway GSL (Belovsky et al., 2011).

GSL has fluctuated between 7.6 m and 13.7 m deep over the historical record (1847-present) (Belovsky et al., 2011) with fluctuations during the seasonal cycle of summer evaporation and spring snow melt, interannual variability, and recent declining trends. In August 2022, GSL lake levels reached a historic low at just 6.8 m deep, with a surface elevation of 1,277 m, 3 m below the historic average (Ramirez, 2022). Current drought and diversion of inflowing rivers primarily for agriculture are projected to lead to further declines in lake levels in the coming decades (Wurtsbaugh et al., 2017). The decreasing areal extent of GSL is leaving infrastructure at abandoned shorelines and there are growing concerns over health effects associated with exposed lake bed dust (Null and Wurtsbaugh, 2020; Perry et al., 2019). The increase in salinity is projected to negatively impact the lake ecosystem, which will be detrimental to migratory shore and water birds (Jewell, 2021; Sorensen et al., 2020). Changing salinities and lake access will also affect existing resource extraction, including the brine shrimp cyst and mineral extraction industries (Naftz, 2017; Wurtsbaugh et al., 2017). This study seeks to generate Holocene paleolimnological reconstructions that extend beyond the instrumental record to provide longer baselines against which current trends can be compared.

2. Age model

Bowen et al. (2019) measured the radiocarbon of various materials (including brine shrimp cysts, algal mats, *n*-alkanes, carbonate, total organic carbon, and terrestrial macrofossils) from the GSL

sediment core GLAD1-GSL00-1B and formulated a radiocarbon age model based upon the cysts only (n = 15 dates). While some components are older (carbonates) or younger (charcoal), we are interested in all the organics that formed in the lake waters as age control for the lake biomarker-based record. In addition to cysts, the short chain *n*-alkanes, algal mats, and total organic carbon (TOC) all appear to form in lake waters. Thus, these additional age constraints are used to inform a revised age model here (n = 27 dates, **Figure 2a**), which is modestly different from the prior age model (**Figure 2b**). The revised age model is retained, as it has the most constraints. Despite producing older ages (≤300 years) between 5.5 and 3 ka (**Figure 2c**), this is trivial for the 220-year resolution of this study but represents uncertainty on the timing of the 5.5 ka transition identified in this study.

3. Materials and methods

3.1. Lipid extraction

We subsampled sediment core GLAD1-GSL00-1B at 30 cm intervals (approximately every 220 yrs) with each sample spanning ~1 cm (integrating ~7 yr) and samples were stored frozen at –20ºC until analysis. Sediment samples (~10 g) were freeze-dried then homogenized with a mortar and pestle. Total lipid extracts (TLE) were obtained for each sample by immersion in 9:1 dichloromethane (DCM):methanol (MeOH) at 100°C and 1.034×10^4 kPa for 15 min using a Dionex ASE 350 Accelerated Solvent Extraction at the University of Southern California.

3.2. GDGT quantification

TLEs were dissolved in 40 µL 99:1 hexane:isopropanol and filtered through 0.45 µm PTFE (polytetrafluoroethylene) filters. 10 µL (or ¼ of the sample) was injected and archaeol, isoGDGTs, and brGDGTs were separated using an Agilent 1260 Infinity high-performance liquid chromatograph (HPLC) coupled to an Agilent 6120 single quadrupole mass spectrometer with two Ethylene Bridged Hybrid (BEH) Hydrophilic Interaction (HILIC) silica columns (2.1 mm × 150 mm, 1.7 µm; Waters) in series at 30°C following the methods of Hopmans et al. (2016). The mobile phase is hexane:isopropanol with a linear gradient transition between 98.2:1.8 for 25 mins, 96.5:3.5 for 25 mins, 90:10 for 50 mins, and reverting to the initial mixture for 20 mins, for a total of 120 minutes at a flow rate of 0.20 mL min^{-1}. Ionization was via positive ion atmospheric pressure chemical ionization (APCI) and detection was in selective ion

194 monitoring (SIM) mode, targeting the *m/z* for archaeol (653.8), isoGDGTs (1302.3, 1300.3,
195 1298.3, 1296.3, 1292.3), and bGDGTs (1050.0, 1048.0, 1046.0, 1036.0, 1034.0, 1032.0, 1022.0,
196 1020.0, 1018.0) at a mass tolerance of 1 dalton. Integration of peak areas was done using the
197 MATLAB package ORIGAmI and each compound was quantified by comparison to the peak
198 area for 500 ng of a C_{46} internal standard (*m/z* 743.8) from the University of Arizona (Huguet et
199 al., 2006). Six samples were rerun in SIM mode with an additional target to detect extended
200 archaeol (*m/z* 723.8), injecting 10 µL out of 200 µL as it is an abundant compound, but otherwise
201 using the same conditions. We compared the raw concentrations of summed branched and
202 summed isoprenoidal compounds (ΣisoGDGT and ΣbrGDGT) in ng/g sediment, to assess the
203 productivity of each compound class. Here, we also include 7-methyl isomers (isomers with
204 methyl groups bonded in the C_7 position) in the ΣbrGDGT calculations due to their high
205 abundance in this hypersaline environment (Wang et al., 2021). An example chromatogram is
206 shown in **Figure S1**.

207 The ACE index, a paleosalinity proxy, was calculated using the following equation from Turich
208 and Freeman (2011):

209 $$ACE = \frac{archaeol}{archaeol + GDGT{-}0} \times 100 \quad (1)$$

210 ACE values were converted to salinity according to the calibration of Turich and Freeman
211 (2011), where:

212 $$ACE = 0.35 \times salinity - 5.4 \quad (2)$$

213 We also monitored for extended archaeol, biomarker specific to halophilic *Euryarchaeota*, in a
214 subset of samples (Bale et al., 2019; Vandier et al., 2021) and calculate the ratio R_{EA} following
215 Vandier et al. (2021):

216 $$R_{EA} = \frac{extended\ archaeol}{archaeol + extended\ archaeol} \quad (3)$$

217 The MBT'_{5Me} index, a brGDGT temperature proxy, was calculated according to De Jonge et al.
218 (2014a):

$$MBT'_{5Me} = \frac{Ia+Ib+Ic}{Ia+Ib+Ic+IIa+IIb+IIc+IIIa} \quad (4)$$

where I-III indicates the number of methyl groups (4-6), and a-c the number of cyclopentane rings (0-2). While MBT'_{5Me} is most frequently used as an indicator for temperature, recent work by Martinez-Sosa et al. (2021) and Wang et al. (2021) found evidence that salinity, particularly hypersalinity, may bias temperature estimates. We convert the MBT'_{5Me} values to mean annual temperature for months above freezing (MAF) using $BayMBT_0$, the Bayesian calibration of Dearing Crampton-Flood et al. (2020) available for both global surface soils and lake sediments. Martinez-Sosa et al. (2021) suggested that alkaline, saline lakes may receive greater brGDGT input from surrounding soils than from in lake production. Thus, we test both the soil and lake calibrations here.

The CBT′ index is used as a pH indicator and was also calculated following the equation of De Jonge et al. (2014a):

$$CBT' = log_{10}\left(\frac{Ic+IIa'+IIb'+IIc'+IIIa'+IIIb'+IIIc'}{Ia+IIa+IIIa}\right) \quad (5)$$

where ′ denotes structural isomers with methyl groups bonded in the C_6 rather than C_5 position. We calculated pH values using the global soils and lakes calibrations of Raberg et al. (2022):

$$CBT' = 0.50 \times soil\ pH - 3.65 \quad (6)$$

$$CBT' = 0.23 \times lake\ pH - 1.98 \quad (7)$$

As the CBT′ formulation in Raberg et al. (2022) included a negative sign, both calibration equations were adjusted to maintain the positive formulation of CBT′ (equation 5) as originally defined by De Jonge et al. (2014a).

The IR_{6Me} index is the ratio of 6-methyl brGDGT isomers to the sum of 5- and 6-methyl brGDGT isomers, calculated according to De Jonge et al. (2014b):

$$IR_{6Me} = \frac{IIa'+IIb'+IIc'+IIIa'+IIIb'+IIIc'}{IIa+IIb+IIc+IIIa+IIIb+IIIc+IIa'+IIb'+IIc'+IIIa'+IIIb'+IIIc'} \quad (8)$$

242 The fractional cyclization (fC) index shows the proportion of brGDGTs with cyclopentane rings
243 and is calculated according to Martinez-Sosa and Tierney (2019):

244 $$fC = \frac{\sum(b)+2\sum(c)+\sum(b')+2\sum(c')}{\sum(a)+\sum(b)+\sum(c)+\sum(b')+\sum(c')} \times 0.5 \quad (9)$$

245 The branched and isoprenoidal tetraether (BIT) index measures the proportion of branched to
246 isoprenoidal inputs, with the isoprenoidal inputs represented only by crenarchaeol. BIT is
247 calculated using the equation of Hopmans et al. (2004):

248 $$BIT = \frac{Ia+IIa+IIa'+IIIa+IIIa'}{Ia+IIa+IIa'+IIIa+IIIa'+cren} \quad (10)$$

249 However, BIT is limited in environments where crenarchaeol is a minor constituent; in such
250 cases it may be more useful to compare the summed branched and isoprenoidal compounds using
251 the ratio $R_{i/b}$:

252 $$R_{i/b} = \frac{\Sigma isoGDGT}{\Sigma brGDGT} \quad (11)$$

253 BIT was originally developed as a measure of terrestrial GDGT input to marine environments,
254 but recent work by Xiao et al. (2016) introduced the ΣIIIa/ΣIIa ratio as a measure solely of
255 brGDGT sourcing without including crenarchaeol:

256 $$\Sigma IIIa/\Sigma IIa = \frac{IIIa+IIIa'}{IIa+IIa'} \quad (12)$$

257 Martin et al. (2020) and Ramos-Roman et al. (2022) later extended this to lacustrine
258 environments and included the 7-methyl isomers (denoted by ″):

259 $$\Sigma IIIa/\Sigma IIa = \frac{IIIa+IIIa'+IIIa''}{IIa+IIa'+IIa''} \quad (13)$$

260 **4. Results**

261 We measured the individual isoGDGT and brGDGT abundances along with archaeol abundance
262 (data available at NOAA; So et al., 2022). IsoGDGTs are dominated by GDGT-0 (**Figure 3a**)

and we show the distribution of the remaining isoGDGTs (**Figure 3b**). ΣisoGDGT and ΣbrGDGT were similar in magnitude (**Figure 3c**). ΣisoGDGT values had a mean of 168 ng/g (1σ = 56 ng/g) and ΣbrGDGT values had a mean of 117 ng/g (1σ = 39 ng/g). Only 5 out of the 35 samples had ΣbrGDGT exceeding ΣisoGDGT (by <30 ng/g).

The salinity proxy, the Archaeol and Caldarchaeol Ecometric (ACE), remained relatively invariant throughout the record with a mean of 90.5 (1σ = 3.7) from 7.2 ka to present; Z-scores range from -2.5 to 2.0 (**Figure 4a**). Statistical analysis using the R Package EnvCpt (Beaulieu and Killick, 2018) for environmental time series changepoint detection confirms a single changepoint in the mean and variance for the MBT'_{5Me} index between a mean of 0.49 (1σ = 0.05) before 5.5 ka to a mean of 0.67 (1σ = 0.05) from 5.5 ka to present (**Figure 4b**, **Figure S2b**). The same changepoint analysis identified shifts at the same time in other indices as follows. IR_{6Me} values showed a small increase from 0.61 (1σ = 0.02) before 5.5 ka to 0.69 (1σ = 0.03) after (**Figure 4c**, **Figure S2c**). The fC index shifted from 0.23 (1σ = 0.02) before 5.5 ka to 0.15 (1σ = 0.03) after (**Figure 4d**, **Figure S2d**). The ΣIIIa/ΣIIa ratio including 7-methyl isomers remained constant over 7.2 ka (**Figure 4e**), averaging 0.84 (1σ = 0.13). However, when 7-methyl isomers are excluded, a step shift at 5.5 ka is seen, with ΣIIIa/ΣIIa averaging 0.64 (1σ = 0.08) pre-shift and 0.38 (1σ = 0.06) post-shift (**Figure S2e**). Additional indices were relatively invariant. CBT′ values averaged -0.01 (1σ = 0.08) across the record (**Figure S3c**). The BIT index was high and invariant across 7.2 ka (**Figure S3f**), with a mean of 0.95 (1σ = 0.02). $R_{i/b}$ averaged 1.51 (1σ = 0.05) across 7.2 ka, indicating archaeal isoGDGTs are generally more abundant than bacterial brGDGTs (**Figure S3g**). As ACE was relatively insensitive, we measured extended archaeol in six samples. We found R_{EA} was as high as 40% prior to 5.5ka (mean 20%, 1σ = 12%) and consistently low after 5.5 ka (mean 6%, 1σ = 3%) (**Figure 4a**).

5. Discussion

5.1. GSL Holocene paleosalinity

Measured ACE values for the Holocene GSL interpreted with the calibration of Turich and Freeman (2011) indicate a mean salinity of 274 g/L (1σ = 11 g/L) with <50 g/L of variability for the whole record. Thus, from 7.2 ka to present, we find GSL to be hypersaline and its salinity to be relatively invariant (**Figure 5**). The low variability (<50 g/L) likely results from applying the

ACE index at its upper limits. With all samples having ACE values >80 (almost all archaeol with little GDGT-0), the index would have limited sensitivity to variations at such high salinities. At deeper depths in the same GLAD core that extends through Pleistocene pluvials, the ACE proxy could be applied to study a larger range of salinities. However, in the Holocene hypersaline terminal lake system, we approach the upper limit of the index.

Modern lake measurements indicate the salinity of the North Arm brine is over 300 g/L, and the South Arm brine is close to 140 g/L (the latter being more reflective of GSL prior to causeway separation). Historical measurements (data for 1966-2020, Rupke and McDonald, 2012) indicate the salinity range of surface samples and depth profiles in the North Arm is 250-340 g/L and the South Arm is 100-220 g/L. Although the available ACE calibration (Turich and Freeman, 2011) suggests salinities in the range of 248-295 g/L during the mid to late Holocene, these estimates appear too high, as this is higher than the modern and historical measurements for the South Arm, with such values found only in the North Arm today. Overestimates of salinity using ACE (values ranging 14-67) have previously been reported in the Piedmont Basin (Italy), which was deposited at the onset of the Miocene Messinian salinity crisis (Natalicchio et al., 2017). This was attributed to archaeol and GDGT-0 production by methanotrophic *Euryarchaeota* and *Thaumarchaeota* in addition to halophilic archaea. In the Holocene GSL, the *Euryarchaeota* are likely producers based on high GDGT-0 and low crenarchaeol (**Figure 3a**).

Absolute salinities are therefore approximations given the limited datasets for calibration and the lack of laboratory quantification standards for each of the analytes. Turich and Freeman (2011) noted that HPLC-MS measurements made in different laboratories have differential ionization of archaeol and GDGT-0, which Natalicchio et al. (2017) also noted. Given the present lack of robust quantification and comparability, we interpret the ACE index as a qualitative indicator of salinity. In addition to relative response factors, the different ecologies of different aquatic communities and their limited calibration each affect the quantitative interpretation of the proxy at present. We can rule out low GDGT-0 relative response factors based on analyses with the same instrument conditions in other sedimentary archives across the full range of the ACE index (Feakins et al., 2019; Peaple et al., 2021). In the Holocene GSL, we may expect some archaeol and GDGT-0 production by halophilic methanogens but not *Thaumarchaeota* given the high GDGT-0/crenarchaeol ratios (based on the inferences of Natalicchio et al. (2017)). Instead, the

dominant producers are likely methanogenic *Euryarchaeota*, which can be indicative of stratified waters (Baxter et al., 2021; Blaga et al., 2009; Naeher et al., 2014). The narrow range and consistently high calculated ACE values of 80-100 suggest limited microbial ecology variability or a loss of sensitivity to salinity variations near the index maximum.

We can also test the ACE salinity proxy through comparison to other evidence for hypersalinity. Bowen et al. (2019) found brine shrimp cysts throughout the core section. In modern GSL, brine shrimp are abundant in the south arm and previous studies have identified the optimum salinity range for these shrimp to be 120-160 g/L, below which brine shrimp are limited by predation and above which by physiological stress (Great Salt Lake Salinity Advisory Committee, 2021). The presence of cysts seems to indicate ACE overestimates salinity. However, there are likely spatial and temporal differences between ACE and cysts as salinity recorders as we will explore. Brine shrimp live in shallow, marginal shore environments while their cysts float near the surface and can be transported/deposited in deeper parts of the lake. In comparison, halophilic archaea can be found throughout the water column and may record salinities at different depths including the saltier deep water at density stratified times. Seasonally, brine shrimp become very productive in late spring when temperatures reach 18-20°C while archaea may be most productive during the warm summer. Thus, high ACE values may not indicate a calibration problem for this system and instead the mismatch between high ACE and cyst may reflect seasonally varying or depth stratified salinity.

A biomarker more specific to halophilic archaea, but that has not yet been developed into a quantitative proxy, is extended archaeol (Bale et al., 2019; Vandier et al., 2021). We measured extended archaeol for six samples (three pre-5.5 ka, three post-5.5 ka) and detect this compound in all six. We calculate R_{EA}, defined by Vandier et al. (2021) as the ratio of extended archaeol to the sum of extended archaeol and archaeol, and find R_{EA} to range from 3-30%, with the pre-5.5 ka average being 20% (1σ = 12%) and the post-5.5 ka being 6% (1σ = 3%) (**Figure 4a, 5b**). The presence of this compound confirms the presence of abundant halophilic *Euryarchaeota*. Vandier et al. (2021) broadly identifies an increase in R_{EA} with an increase in salinity and this, together with generally higher R_{EA} pre-5.5 ka, may suggest higher salinities during the arid mid-Holocene. However, as extended archaeol is a relatively novel compound and its abundance

cannot currently be directly converted to salinity values, further studies are needed to validate this interpretation.

Overall, both high ACE values, constant brine shrimp cyst presence, and high quantities of extended archaeol indicate GSL hypersalinity over the past 7.2 ka. Given that GSL ACE values extend beyond the upper limits of the calibration of Turich and Freeman (2011) and the lack of an applicable local calibration, the calculated salinities may be overestimates and we consider reconstructions to be semi-quantitative using existing ACE calibrations. The limited variability detected by ACE suggests a role for an additional hypersalinity marker, extended archaeol to discern variations in extreme salinity in this setting.

5.2. MBT′$_{5Me}$ temperature record

Using the BayMBT$_0$ lake calibration, the mean annual temperature of months above freezing (MAF) averaged 18°C (1σ = 3°C) throughout the record, with a mean of 15°C (1σ = 2 °C) before 5.5 ka and 20°C (1σ = 2 °C) after (**Figure 6**). Lower MAF estimates resulted from the soil calibration, averaging 14°C (1σ = 3°C) throughout the record, 10°C (1σ = 2°C) before 5.5 ka, and 15°C (1σ = 2°C) after 5.5 ka. After the step change at 5.5 ka, the soil-based calibration yields MAF estimates that closely match those of present-day Salt Lake City (15.7°C; National Centers for Environmental Information, 2022), whereas the lake-based calibration yielded temperatures that were on average 4°C too warm. A warm bias for saline lakes had previously been reported from the global lakes calibration dataset including nearby Mono Lake, California (Martinez-Sosa et al., 2021).

Reconstructed temperatures apparently increased by 5°C at 5.5 ka (**Figure 6**). Temperatures reconstructed using the soil calibration before 5.5 ka were much cooler than expected when compared against modern temperatures, whereas using the lake calibration temperatures were similar to modern. Previous climate records suggest the mid-Holocene to be a warm, arid period relative to the late Holocene and no known climatic processes would support a step change in MAF of that magnitude at that time (see **Section 5.4**). As we also detect a step shift at 5.5 ka in several GDGT indices (see **Section 5.3** and **Figure S2**), it is likely that non-thermal changes in GSL at 5.5 ka affected the MBT′$_{5Me}$ proxy, whether through a change in the microbial community between a saltier, shallower lake and a deeper lake with increased overturning and

bottom water oxygenation, and/or a shift in the productivity within the lake, and/or changes in the influx of microbial lipids from surrounding soils. We do find evidence from extended archaeol relative to archaeol that the pre-5.5 ka GSL was saltier (**Figure 5b**). We also find an increase in IR_{6Me}, decrease in fC, and decrease in ΣIIIa/ΣIIa excluding 7-methyl isomers, which also point to a shift in the microbial community and their lipids within the lake. Whereas exploration of soil versus lake provenance is, to some extent, inconclusive (see supplementary), some of the questions remain unclear and signal a need for more regional calibration of microbial communities in saline lake systems. While we are not certain about the nature of the microbial community change, we see signs of non-thermal factors and we do not interpret the temperatures for 7.2-5.5 ka (**Figure 6**, yellow shading).

5.3. Limnology shift at 5.5 ka

Although the ACE index may be relatively insensitive to salinity change in the last 7.2 ka given the hypersalinity of the lake, other biomarker indices show evident changes. Changepoint analysis revealed a shift in several GDGT indices that indicate shifts in limnological conditions at 5.5 ka (MBT'_{5Me}, IR_{6Me}, fC, and ΣIIIa/ΣIIa) (**Figure 4**, **Figure S2**). We see an increase in MBT'_{5Me} values at 5.5 ka (**Figure 4b**). As MBT'_{5Me} is a paleotemperature proxy, these values alone would indicate increased temperatures. The increase in IR_{6Me} at this time means a proportional increase in 6-methyl brGDGT isomers (**Figure 4c**). Greater proportions of 6-methyl isomers have been linked to higher pH (De Jonge et al., 2014a; Raberg et al., 2021; Raberg et al., 2022), comparatively more aquatic production than soil production (De Jonge et al., 2014b; Kirkels et al., 2020), lower soil water content (Dang et al., 2016), and/or higher conductivity (Raberg et al., 2021). A decrease in fC is a decrease in the proportions of cyclized brGDGTs (**Figure 4d**). Less cyclization of brGDGTs has been linked to lower pH/conductivity (Raberg et al., 2021), and/or comparatively more soil production (Kirkels et al., 2020). We also see a step decrease at 5.5 ka in ΣIIIa/ΣIIa values when 7-methyl isomers are excluded (**Figure 4e**). Lower ΣIIIa/ΣIIa values indicates a lower proportion of brGDGTs with six methyl groups compared to those with five methyl groups and has been linked to increased soil inputs to lacustrine environments (Martin et al., 2020; Ramos-Roman et al., 2022). However, when 7-methyl isomers are accounted for, the ΣIIIa/ΣIIa ratio remains relatively constant. Principal component

analysis (PCA) of GSL samples further supports a shift in lake conditions at 5.5 ka with samples pre- and post-5.5 ka plotting in separate clusters (**Figure S4a**).

MBT'_{5Me} values are low prior to this shift and, using the soil calibration, yield unrealistically cold temperatures (**Figure 6**). Lake production of brGDGTs has a 'colder' distribution than soils (Martinez-Sosa et al., 2021), thus a shift to *in situ* aquatic production might explain the observed pattern. The values pre-5.5 ka may instead represent more *in situ* lake production of brGDGTs during the middle Holocene, making it more appropriate to use the lake calibration and this seems to be supported by lake calibration temperatures matching more closely to modern Salt Lake City temperatures during this time. One possibility is that lower lake levels prior to 5.5 ka combined with arid conditions restricted river inflows that would have brought soil-produced brGDGTs to GSL. Mixed brGDGT sourcing is possible for Holocene GSL based on its distributions of tetra-, penta-, and hexamethylated brGDGTs (Ramos-Roman et al., 2022; Russell et al., 2018) falling between those of global lakes and soils (**Figure S5, S6**), although neither pre- nor post-5.5 ka distributions can be unambiguously ascribed to a purely lake-like or soil-like signal compared to large global datasets (**Figure S4b, S6**). Thus, we do not find strong support for a shift from lake to soil-derived compounds.

Part of the ambiguity may be due to the uniqueness of GSL. PCA analysis shows that GSL has an extreme brGDGT distribution compared to global distributions, especially prior to 5.5 ka (**Figure S4b**). Hypersaline lakes differ in their chemistry and are isolated bodies of water which may have fundamentally different microbial communities and/or lipid responses to environmental change than their freshwater counterparts or other saline lakes. Wang et al. (2021) noted warm-biased MBT'_{5Me} values with increasing salinity. In contrast to Martinez-Sosa et al. (2021) who had attributed this warm bias to soil inputs, Wang et al. (2021) attributed this to increased production of 7-methyl penta- and hexamethylated isomers in place of 5-methyl ones by lake microbes. This would explain the temperature overestimates we observe when using the $BayMBT_0$ lake calibration post-5.5 ka (**Figure 6**). Overall, both studies indicate warm biases in MBT'_{5Me} in saline lakes, although the variations need additional study.

Across the 5.5 ka transition, IR_{6Me} and fC increase and decrease respectively (**Figure 4c, 4d**). pH estimated from CBT′ using the soil calibration of Raberg et al. (2022) averaged 7.2 ($1\sigma = 0.02$)

and using the lake calibration averaged 8.6 ($1\sigma = 0.03$). Both calibrations yield near-constant pH values throughout the whole record meaning shifts in IR_{6Me} and fC are likely not due to changes in pH. Pre-5.5 ka, higher fC could indicate higher conductivity which may reflect higher temperature and/or higher salinity, both of which align with middle Holocene aridity (see **Section 5.4**). Lower IR_{6Me} values are harder to reconcile as they would suggest lower conductivity, opposite that of fC. Aside from conductivity, low IR_{6Me} may otherwise indicate higher soil water content and/or a greater influx of organic material produced in soils. However, these factors seem secondary to pH and conductivity as controls of IR_{6Me}. Additionally, an interpretation of high soil water content or soil production would contrast with both regional climate records, which highlight mid-Holocene aridity, and brGDGT provenance studies, which do not suggest shifts from lake to soil sourcing. Due to the large number of factors with potential to influence IR_{6Me} at this site, we do not interpret the exact environmental implications of the IR_{6Me} step change.

The decrease in ΣIIIa/ΣIIa values with the exclusion of 7-methyl isomers would suggest greater soil input after 5.5 ka, but constant values when these isomers are included indicate otherwise (**Figure 4e**). Throughout the 7.2 ka record, the quantity of 7-methyl isomers is comparable to or exceeds their 5- and 6-methyl counterparts. Wang et al. (2021) reported high abundances of 7-methyl isomers in hypersaline lakes and low amounts in freshwater lakes. The high abundance of 7-methyl isomers at hypersaline GSL may explain the trends in the different formulations of ΣIIIa/ΣIIa (**Figure 4e**). It is likely that 7-methyl brGDGTs are produced within the hypersaline lake and their high abundance results in differing ΣIIIa/ΣIIa trends when these isomers are included or excluded. The coincident changepoint in four GDGT indices (MBT'_{5Me}, IR_{6Me}, fC, and ΣIIIa/ΣIIa) (**Figure 4**, **Figure S2**) suggests a change in both the bacterial and archaeal communities suggesting that the microbial and limnological conditions of GSL pre-5.5 ka are distinct from post-5.5 ka.

Our biomarker reconstruction detects a changepoint in GSL limnology at 5.5 ka in several metrics and those non-thermal effects appear to disrupt the temperature proxy. Though ACE shows that GSL is hypersaline throughout the 7.2 ka record, both high ACE and extended archaeol show that the mid-Holocene lake was saltier and shallower than the subsequent 5.5 ka.

We infer that the shallower, saltier mid-Holocene lake hampered paleothermometry in this time, while the late Holocene temperature reconstructions appear reasonable.

5.4. Comparison to regional climate

The reconstruction of shallower, saltier (**Figure 7a**) GSL in the mid-Holocene is consistent with evidence for regional aridity. In Lehman Caves (NV) located 260 km southwest of GSL, a decrease in speleothem Mg/Ca shows increased aridity at ~8 ka (Steponaitis et al., 2015) (**Figure 7b**). In nearby Leviathan Cave (NV) 180 km southwest of GSL, a decrease in speleothem $\delta^{13}C$ values at ~4 ka is interpreted as an increase in effective moisture (Lachniet et al., 2020) (**Figure 7c**). Collectively, these cave records bracket a mid-Holocene arid period from around 8-4 ka. A proxy synthesis and reanalysis effort across western North America (Routson et al., 2022) identifies a mid-latitude moisture increase in this region after 6 ka (**Figure 7d**). Preceding this moisture increase, we observe low lake levels in many Great Basin lakes (Steponaitis et al., 2015) (**Figure 7e**), including Owens Lake (CA) (Bacon et al., 2020), Lake Tahoe (CA/NV) (Benson et al., 2002), and Pyramid Lake (NV) (Benson et al., 2002), as well as at small lakes in the Midwest (Shuman et al., 2002) and in the sub-alpine region of the Rocky Mountains (Shuman and Serravezza, 2017). A compilation of southwestern US climate records by Lachniet et al. (2020) also found peak aridity at 7.5 ka (**Figure 7f**). Thus, it seems likely that widespread mid-Holocene aridity in mid-latitude western North America contributed to a shallower GSL recorded from the start of this record at 7.2 ka to 5.5 ka, with a shift to wetter conditions represented locally at 5.5 ka.

Most of the precipitation in the Great Basin falls during the winter with moisture delivered by westerlies from the Pacific, and a much smaller fraction falls during the summer as part of the North American Monsoon (NAM) with moisture from the Gulf of California and eastern Pacific (Lachniet et al., 2020). Moisture from the Gulf of Mexico can also contribute to the NAM, but this rarely reaches the Great Basin (Jana et al., 2018). Changes in the incursion of the NAM and the position of westerlies over western North America have been inferred from the reanalysis of a large network of proxy data (Routson et al., 2022). They identified a strong NAM that peaked at 7 ka, coincident with weakened/northward-deflected westerlies. The latter could explain the dry mid-Holocene in the mid-latitudes, including at GSL from 7.2 to 5.5 ka, as it would have

decreased delivery of Pacific moisture. Following this, in the late Holocene, a reduction in the NAM and more zonal westerly flow, resulted in wetter conditions in western North America including at GSL.

Routson et al. (2022) suggested that these changes in circulation were linked to meridional temperature gradients. Changes in broad scale atmospheric circulation and Pacific SSTs due to high summer insolation and Laurentide ice sheet (LIS) collapse have previously been connected to Holocene shifts in the precipitation regime over the western US. Summer northern hemisphere insolation peaked in the Early Holocene ~11-10 ka and has steadily decreased up to the present (Lachniet et al., 2020). In the same time period, the LIS rapidly retreated from 10-8 ka (Shuman et al., 2002), mostly having disappeared by ~7 ka (Peltier et al., 2015). Steponaitis et al. (2015) attributed the onset of mid-Holocene aridity in the Great Basin at ~8 ka to a northward displacement of winter storm tracks after the collapse of the remnant LIS. In contrast, Lachniet et al. (2020) suggested summer insolation to be the primary driver of regional climate variation. They find a connection between southwestern US drought and increased SSTs in the western tropical Pacific (WTP), warmth in the Arctic, and low Arctic sea ice, these phenomena being caused by high summer insolation. Both Steponaitis et al. (2015) and Lachniet et al. (2020) also suggest that a La Niña-like configuration of the tropical Pacific (a response to orbital forcing (Brierley et al., 2020) may have contributed to regional aridity.

Changes in summer insolation and the LIS have also been linked to hydroclimate changes in other regions of the US. Lake and pollen records indicate a moist to dry transition in the Midwest, and a dry to moist transition in the northeast and southeast between 9 and 8 ka, attributed to the collapse of the LIS Hudson Bay Dome and the subsequent proportional increase in the influence of summer insolation (Shuman et al., 2002). In the northeast, plant wax isotopes show an increased ratio of summer to winter precipitation after 8 ka, as the LIS glacial anticyclone previously prevented northward transport of subtropical moisture during the summer (Shuman et al., 2006). From ~9-7 ka, lakes in California, the Great Basin, and the Rocky Mountains declined while those in western Canada rose. These trends reversed by ~5.7 ka, possibly due to the decline in summer insolation after the LIS melted (Shuman and Serravezza, 2017). Similarly, between 5.7-5.2 ka, lakes across central and eastern mid-latitude North America show an increase in effective moisture, which terminated mid-Holocene aridity and

coincided with the end of the Holocene temperature maximum in this region (Shuman and Marsicek, 2016). A global compilation of Holocene temperature proxies ("Temperature 12K") including their age model uncertainties, places the central estimate for mid-Holocene warmth around 6.45 ka within a range of 7.65-4.95 ka (Kaufman et al., 2020).

Model studies also suggest similar patterns of mid-Holocene aridity driven by large scale climatic processes. Diffenbaugh et al. (2006) found insolation to be the primary driver of North American midcontinent aridity and model efforts by Shin et al. (2006) suggested persistent La Niña-like Pacific SST patterns (i.e. warm western tropical Pacific, cool eastern tropical Pacific). Bhattacharya et al. (2018) found both models and proxy records from the Gulf of California region indicate a weakened NAM during the last glacial and NAM strengthening as the LIS retreated and westerly storm tracks, which previously mixed in cold, dry air that weakened the NAM, were displaced/weakened. While the LIS had largely disappeared by the middle Holocene, PMIP4-CMIP6 simulations still show enhanced seasonality and stronger monsoons in the northern hemisphere compared to preindustrial times (Brierley et al., 2020). The model dynamics support the proxy evidence for a strong NAM and weakened westerlies in the middle Holocene, leaving dry conditions in mid-latitude western North America (Routson et al., 2022). In the late Holocene, once NAM weakened, the more zonal westerlies (Routson et al., 2022) may have increased the moisture flux to the GSL region, resulting in the more mesic conditions experienced until recently.

The late Holocene was comparably wetter than the mid-Holocene, with lake high stands from ~4.5 to ~3 ka recorded at Owens Lake (CA) (Bacon et al., 2020; Benson et al., 2002), Walker Lake (NV) (Benson et al., 1991), Pyramid Lake (NV) (Briggs et al., 2005), Winnemucca Lake (NV) (Briggs et al., 2005), Mono Lake (CA) (Stine, 1990), and Silver Lake (CA) (Enzel et al., 1989). Although the biomarker record was stable without changepoints within the late Holocene, we do observe some variability within the GSL record. We note an ACE spike at 2.8 ka (**Figure 7a**) so this may have been a short lived drying in GSL. This may correspond to the onset of the Late Holocene Dry Period (2.8-1.85 ka) identified by Mensing et al. (2013) with lake low stands at Mono Lake (CA) (Stine, 1990), Walker Lake (CA) (Adams, 2007; Benson et al., 1991), Zaca Lake (CA) (Kirby et al., 2014), and Bear Lake (UT/ID) (Moser and Kimball, 2009). Tree ring studies are optimal for shorter timescales with limber pine assemblages in the western Great

Basin spanning the last 4000 years (Millar et al., 2019). Within the Late Holocene Dry Period, they found wet interludes occurred at the Neoglacial and Little Ice Age, whereas drought conditions stunted tree growth in the last 20 years, the second driest interval in the last 4000 years, surpassed only during 20 BC to 150 AD (Millar et al., 2019). The 220-year resolution of sampling in this study of GSL is not sufficient to contribute to finer records of hydroclimate (20-200 yr droughts). Although finer sampling is possible (samples span 1 cm, integrating ~7 yrs), there are limits to the resolution in lake sediments in a large lake with a large catchment, for example terrestrial plant wax, may experience considerable pre-aging on the landscape (Bowen et al., 2019) that may preclude detailed Holocene reconstructions. Longer records are the focus of future study as the GLAD drilling extended to 175 ka, capturing Pleistocene pluvials that may be resolved by the ACE salinity proxy which had approached its upper limit for the Holocene hypersaline terminal lake system.

6. Conclusions

We reconstructed a Holocene paleoclimate record for GSL using GDGT biomarker analyses of lacustrine sediments from the GLAD1-GSL00-1B sediment core spanning 7.2 ka to present. Although absolute salinity interpretations of the ACE index in GSL are uncertain, the index is near its upper limit (>80/100) suggesting that hypersaline conditions existed throughout the record. Applying the calibration of Turich and Freeman (2011), ACE values in these Holocene GSL sediments suggest salinities >250 g/L, though comparison to the present-day salinity range along with brine shrimp cyst evidence suggests this may be an overestimate, or represent spatial or temporal differences between the two recorders.

For the brGDGT thermometer, the BayMBT$_0$ soil calibration yielded MAF estimates consistent with modern Salt Lake City MAF from 5.5 ka to the present, whereas the lake calibration was warm-biased, consistent with reports of saline lake outliers in prior calibration studies (Martinez-Sosa et al., 2021). In contrast, the soil calibration yields unreasonably cold temperatures during the mid-Holocene while the lake calibration yields temperatures similar to modern MAF. Using either calibration alone, at 5.5 ka we find an apparent step shift in temperature of 5ºC. However, such a large, abrupt warming is unlikely as the Holocene is a generally stable time. As we do not find provenance evidence to support a switch in calibration for the MBT′$_{5Me}$ index, we maintain

585 interpretations of the late Holocene temperature records that are consistent with modern MAF,
586 but we do not find temperature estimates to be secure for the mid-Holocene.

587 Changepoint analysis reveals that several other GDGT indices (IR_{6Me}, fC, ΣIIIa/ΣIIa without 7-
588 methyl isomers) also show a step shift at 5.5 ka strongly suggesting non-thermal effects on
589 MBT'_{5Me}, likely a change in the lake depth influencing microbial communities before 5.5 ka. We
590 find some support from extended archaeol measured on a subset of samples that found greater
591 salinity before 5.5 ka. We interpret these data to indicate a shallow, saltier lake from 7.2 to 5.5
592 ka, in line with regional evidence for dry conditions during the mid-Holocene (Lachniet et al.,
593 2020).

594 This paleolimnological study provides context for recent changes in the instrumental record, with
595 a decline in lake level of 7 m from 1986 to 2022, which has reduced the surface area from 8550
596 km^2 to 2460 km^2 (Utah Department of Natural Resources, 2022) due to unsustainable water use
597 and climate change (Wurtsbaugh et al., 2017). Our biomarker record extends the instrumental
598 baseline against which the current drying can be compared, finding relatively stable conditions at
599 GSL over the last 5.5 ka, with modern conditions approaching that of the mid-Holocene aridity.
600 The mid-Holocene salty and shallow GSL is a prelude to the current changes associated with
601 water extraction and drying.

602 **Acknowledgements**

603 This study was supported by U.S. National Science Foundation Grant NSF-EAR-1903665 to
604 S.F., and the Packard Fellowship for Science and Engineering to J.T. Sample material used in
605 this project was provided by Continental Scientific Drilling Facility. We thank Patrick Murphy
606 for performing GDGT analyses. We thank Yige Zhang, Gabriel Bowen, David McGee, Mark
607 Peaple, Emily Tibbett and Annie Tamalavage for helpful discussions. This manuscript was
608 improved with the helpful comments of three anonymous reviewers.

609 **Supporting Information**

610 Supporting Information may be found in the online version of this article.

611 **Conflict of Interest**

612 The authors declare no financial conflicts of interests for any author or their affiliations.

613 **Open Research**

614 Data files are archived at the NOAA paleoclimatology database (So et al., 2022).

615 **Figure Captions**

616 **Figure 1.** Maps showing a) the Great Salt Lake (GSL) core site of GLAD1-GSL00-1B and the
617 Lake Bonneville shoreline (top right), and b) the locations of regional comparison records.

618 **Figure 2.** Age model based on all lake organic carbon radiocarbon dates (Bowen et al., 2019)
619 from the GLAD core using the Bayesian R package BACON (Blaauw and Christen, 2011). a)
620 Calibrated radiocarbon age probability distribution functions (blue), age model mean (red line)
621 and uncertainty (gray shading), b) comparison between the age model mean (red line) for all lake
622 organic radiocarbon dates (used in this study) and the cyst-only model (blue line) presented by
623 Bowen et al. (2019), and c) their difference. The biomarker transition at 5.5 ka in the all-lake OC
624 model is ~200 years older than in the cyst-only model.

625 **Figure 3.** Change in the distribution and concentration of isoGDGTs in the GSL over the 7.2 ka
626 record, showing a) isoGDGT proportional abundances, b) isoGDGT proportional abundances
627 without GDGT-0, and c) isoGDGT (black) and brGDGT (gray) concentration through time.

628 **Figure 4.** Temporal variations in GDGT indices showing a) ACE Z-score (blue) and R_{EA} (black
629 cross), b) MBT'_{5Me}, c) IR_{6Me}, d) fC, and e) ΣIIIa/ΣIIa. We use statistical methods to identify a
630 changepoint in several indices at 5.5 ka (**Figure S2**). The portion of the record prior to the step
631 change is highlighted (yellow shading).

632 **Figure 5.** Salinity indicators in a 7.2 ka record from GLAD1-GSL00-1B core. a) ACE variations
633 near the upper limit of the index. b) Calculated ACE Z-scores (blue line) and R_{EA} (black cross).
634 Arrow indicates direction of salinity increase.

635 **Figure 6.** GSL mean annual temperature for months above freezing (MAF) calculated using the
636 $BayMBT_0$ lake (blue) and soil (red) calibrations of Dearing Crampton-Flood et al. (2020) are
637 shown a long with one standard deviation uncertainty (light red envelope for soil calibration

638 temperatures, dashed blue lines for lake calibration temperatures). The black line indicates the
639 Salt Lake City mean annual air temperature for months above freezing (MAF). Yellow shading
640 indicates the period when the MBT'_{5Me} proxy was likely affected by different limnological
641 conditions and microbial production, rather than a change in temperature.

642 **Figure 7.** Compilation of regional paleoclimate reconstructions, showing a) GSL ACE Z-score
643 (this study), b) Lehman Caves (NV) Mg/Ca record (Steponaitis et al., 2015), c) Leviathan Cave
644 (NV) $\delta^{13}C$ record (Lachniet et al., 2020), d) precipitation index for mid-latitude western North
645 America (Routson et al., 2022), e) Great Basin lakes with low lake levels (Steponaitis et al.,
646 2015); and f) aridity index for the southwestern US (Lachniet et al., 2020).

647 **References**

648 Adams, K.D. (2007) Late holocene sedimentary environments and lake-level fluctuations at
649 Walker Lake, Nevada, USA. Geological Society of America Bulletin 119, 126-
650 139.10.1130/b25847.1.

651 Bacon, S.N., Jayko, A.S., Owen, L.A., Lindvall, S.C., Rhodes, E.J., Schumer, R.A. and Decker,
652 D.L. (2020) A 50,000-year record of lake-level variations and overflow from Owens Lake,
653 eastern California, USA. Quaternary Science Reviews 238, 25.10.1016/j.quascirev.2020.106312.

654 Bale, N.J., Sorokin, D.Y., Hopmans, E.C., Koenen, M., Rijpstra, W.I.C., Villanueva, L., Wienk,
655 H. and Damste, J.S.S. (2019) New Insights Into the Polar Lipid Composition of Extremely
656 Halo(alkali)philic Euryarchaea From Hypersaline Lakes. Frontiers in Microbiology 10,
657 24.10.3389/fmicb.2019.00377.

658 Baxter, A.J., van Bree, L.G.J., Peterse, F., Hopmans, E.C., Villanueva, L., Verschuren, D. and
659 Damste, J.S.S. (2021) Seasonal and multi-annual variation in the abundance of isoprenoid GDGT
660 membrane lipids and their producers in the water column of a meromictic equatorial crater lake
661 (Lake Chala, East Africa). Quaternary Science Reviews 273,
662 21.10.1016/j.quascirev.2021.107263.

663 Baxter, B.K., Litchfield, C.D., Sowers, K., Griffith, J.D., DasSarma, P.A. and DasSarma, S.
664 (2005) Microbial diversity of Great Salt Lake. Adaptation to Life at High Salt Concentrations in
665 Archaea, Bacteria, and Eukarya 9, 9-+

Beaulieu, C. and Killick, R. (2018) Distinguishing Trends and Shifts from Memory in Climate Data. Journal of Climate 31, 9519-9543.10.1175/jcli-d-17-0863.1.

Belovsky, G.E., Stephens, D., Perschon, C., Birdsey, P., Paul, D., Naftz, D., Baskin, R., Larson, C., Mellison, C., Luft, J., Mosley, R., Mahon, H., Van Leeuwen, J. and Allen, D.V. (2011) The Great Salt Lake Ecosystem (Utah, USA): long term data and a structural equation approach. Ecosphere 2, 40.10.1890/es10-00091.1.

Benson, L., Kashgarian, M., Rye, R., Lund, S., Paillet, F., Smoot, J., Kester, C., Mensing, S., Meko, D. and Lindstrom, S. (2002) Holocene multidecadal and multicentennial droughts affecting Northern California and Nevada. Quaternary Science Reviews 21, 659-682.10.1016/s0277-3791(01)00048-8.

Benson, L.V., Meyers, P.A. and Spencer, R.J. (1991) Change in the size of Walker Lake during the past 5000 years. Palaeogeography Palaeoclimatology Palaeoecology 81, 189-214.10.1016/0031-0182(91)90147-j.

Bhattacharya, T., Tierney, J.E., Addison, J.A. and Murray, J.W. (2018) Ice-sheet modulation of deglacial North American monsoon intensification. Nature Geoscience 11, 848-+.10.1038/s41561-018-0220-7.

Blaauw, M. and Christen, J.A. (2011) Flexible Paleoclimate Age-Depth Models Using an Autoregressive Gamma Process. Bayesian Analysis 6, 457-474.10.1214/ba/1339616472.

Blaga, C.I., Reichart, G.J., Heiri, O. and Damste, J.S.S. (2009) Tetraether membrane lipid distributions in water-column particulate matter and sediments: a study of 47 European lakes along a north-south transect. Journal of Paleolimnology 41, 523-540.10.1007/s10933-008-9242-2.

Bowen, G.J., Nielson, K.E. and Eglinton, T.I. (2019) Multi-substrate radiocarbon data constrain detrital and reservoir effects in Holocene sediments of the Great Salt Lake, Utah. Radiocarbon 61, 905-926.10.1017/rdc.2019.62.

Brierley, C.M., Zhao, A.N., Harrison, S.P., Braconnot, P., Williams, C.J.R., Thornalley, D.J.R., Shi, X.X., Peterschmitt, J.Y., Ohgaito, R., Kaufman, D.S., Kageyama, M., Hargreaves, J.C., Erb,

693 M.P., Emile-Geay, J., D'Agostino, R., Chandan, D., Carre, M., Bartlein, P.J., Zheng, W.P.,
694 Zhang, Z.S., Zhang, Q., Yang, H., Volodin, E.M., Tomas, R.A., Routson, C., Peltier, W.R., Otto-
695 Bliesner, B., Morozova, P.A., McKay, N.P., Lohmann, G., Legrande, A.N., Guo, C.C., Cao, J.,
696 Brady, E., Annan, J.D. and Abe-Ouchi, A. (2020) Large-scale features and evaluation of the
697 PMIP4-CMIP6 midHolocene simulations. Climate of the Past 16, 1847-1872.10.5194/cp-16-
698 1847-2020.

699 Briggs, R.W., Wesnousky, S.G. and Adams, K.D. (2005) Late Pleistocene and late Holocene
700 lake highstands in the Pyramid Lake subbasin of Lake Lahontan, Nevada, USA. Quaternary
701 Research 64, 257-263.10.1016/j.yqres.2005.02.011.

702 Bunce, L., Lowenstein, T. and Jagniecki, E. (2022) Spring, river, and lake water analyses from
703 the Great Salt Lake basin, northern Utah, Utah Geological Survey Report of Investigation. Utah
704 Geological Survey, Salt Lake City, UT, USA.10.34191/OFR-745.

705 Dang, X.Y., Yang, H., Naafs, B.D.A., Pancost, R.D. and Xie, S.C. (2016) Evidence of moisture
706 control on the methylation of branched glycerol dialkyl glycerol tetraethers in semi-arid and arid
707 soils. Geochimica Et Cosmochimica Acta 189, 24-36.10.1016/j.gca.2016.06.004.

708 Dawson, K.S., Freeman, K.H. and Macalady, J.L. (2012) Molecular characterization of core
709 lipids from halophilic archaea grown under different salinity conditions. Organic Geochemistry
710 48, 1-8.10.1016/j.orggeochem.2012.04.003.

711 De Jonge, C., Hopmans, E.C., Zell, C.I., Kim, J.H., Schouten, S. and Damste, J.S.S. (2014a)
712 Occurrence and abundance of 6-methyl branched glycerol dialkyl glycerol tetraethers in soils:
713 Implications for palaeoclimate reconstruction. Geochimica Et Cosmochimica Acta 141, 97-
714 112.10.1016/j.gca.2014.06.013.

715 De Jonge, C., Stadnitskaia, A., Hopmans, E.C., Cherkashov, G., Fedotov, A. and Damste, J.S.S.
716 (2014b) In situ produced branched glycerol dialkyl glycerol tetraethers in suspended particulate
717 matter from the Yenisei River, Eastern Siberia. Geochimica Et Cosmochimica Acta 125, 476-
718 491.10.1016/j.gca.2013.10.031.

719 Dearing Crampton-Flood, E., Tierney, J.E., Peterse, F., Kirkels, F. and Damste, J.S.S. (2020)
720 BayMBT: A Bayesian calibration model for branched glycerol dialkyl glycerol tetraethers in
721 soils and peats. Geochimica Et Cosmochimica Acta 268, 142-159.10.1016/j.gca.2019.09.043.

722 Diffenbaugh, N.S., Ashfaq, M., Shuman, B., Williams, J.W. and Bartlein, P.J. (2006) Summer
723 aridity in the United States: Response to mid-Holocene changes in insolation and sea surface
724 temperature. Geophysical Research Letters 33, 5.10.1029/2006gl028012.

725 Dinter, D., Haskell, B., Valero-Garcés, B., Schnurrenberger, D., Heil, C., Dean, W. and Kruger,
726 N. (2000) GLAD1, GSL SITE 1, in: Schnurrenberger, D., Haskell, B. (Eds.), Initial Reports of
727 the Global Lakes Drilling Program. University of Arizona; Limnological Research Center,
728 University of Minnesota; Northern Arizona University; University of Utah; United States
729 Geological Survey; University of Rhode Island, Graduate School of Oceanography, pp. 12-17

730 Enzel, Y., Cayan, D.R., Anderson, R.Y. and Wells, S.G. (1989) Atmospheric circulation during
731 Holocene lake stands in the Mojave Desert - Evidence of regional climate change. Nature 341,
732 44-47.10.1038/341044a0.

733 Feakins, S.J., Wu, M.S., Ponton, C. and Tierney, J.E. (2019) Biomarkers reveal abrupt switches
734 in hydroclimate during the last glacial in southern California. Earth and Planetary Science Letters
735 515, 164-172.10.1016/j.epsl.2019.03.024.

736 Great Salt Lake Salinity Advisory Committee (2021) Influence of Salinity on the Resources and
737 Uses of Great Salt Lake, Utah Geological Survey Open-File Report. Utah Geological
738 Survey.10.34191/OFR-736.

739 Hopmans, E.C., Schouten, S. and Damste, J.S.S. (2016) The effect of improved chromatography
740 on GDGT-based palaeoproxies. Organic Geochemistry 93, 1-
741 6.10.1016/j.orggeochem.2015.12.006.

742 Hopmans, E.C., Weijers, J.W.H., Schefuss, E., Herfort, L., Damste, J.S.S. and Schouten, S.
743 (2004) A novel proxy for terrestrial organic matter in sediments based on branched and
744 isoprenoid tetraether lipids. Earth and Planetary Science Letters 224, 107-
745 116.10.1016/j.epsl.2004.05.012.

Huguet, C., Hopmans, E.C., Febo-Ayala, W., Thompson, D.H., Damste, J.S.S. and Schouten, S. (2006) An improved method to determine the absolute abundance of glycerol dibiphytanyl glycerol tetraether lipids. Organic Geochemistry 37, 1036-1041.10.1016/j.orggeochem.2006.05.008.

Jagniecki, E., Rupke, A., Kirby, S. and Inkenbrandt, P. (2021) Salt crust, brine, and marginal groundwater of Great Salt Lake's North arm (2019-2021), Utah Geological Survey Report of Investigation. Utah Geological Survey, Salt Lake City, UT, USA.10.34191/RI-283.

Jana, S., Rajagopalan, B., Alexander, M.A. and Ray, A.J. (2018) Understanding the Dominant Sources and Tracks of Moisture for Summer Rainfall in the Southwest United States. Journal of Geophysical Research-Atmospheres 123, 4850-4870.10.1029/2017jd027652.

Jewell, P.W. (2021) Historic low stand of Great Salt Lake, Utah: I Mass balance model and origin of the deep brine layer. Sn Applied Sciences 3, 16.10.1007/s42452-021-04691-5.

Jones, B.F., Naftz, D.L., Spencer, R.J. and Oviatt, C.G. (2009) Geochemical Evolution of Great Salt Lake, Utah, USA. Aquatic Geochemistry 15, 95-121.10.1007/s10498-008-9047-y.

Kaufman, D., McKay, N., Routson, C., Erb, M., Datwyler, C., Sommer, P.S., Heiri, O. and Davis, B. (2020) Holocene global mean surface temperature, a multi-method reconstruction approach. Scientific Data 7, 13.10.1038/s41597-020-0530-7.

Kirby, M.E., Feakins, S.J., Hiner, C.A., Fantozzi, J., Zimmerman, S.R.H., Dingemans, T. and Mensing, S.A. (2014) Tropical Pacific forcing of Late-Holocene hydrologic variability in the coastal southwest United States. Quaternary Science Reviews 102, 27-38.10.1016/j.quascirev.2014.08.005.

Kirkels, F., Ponton, C., Galy, V., West, A.J., Feakins, S.J. and Peterse, F. (2020) From Andes to Amazon: Assessing Branched Tetraether Lipids as Tracers for Soil Organic Carbon in the Madre de Dios River System. Journal of Geophysical Research-Biogeosciences 125, 18.10.1029/2019jg005270.

771 Lachniet, M.S., Asmerom, Y., Polyak, V. and Denniston, R. (2020) Great Basin Paleoclimate
772 and Aridity Linked to Arctic Warming and Tropical Pacific Sea Surface Temperatures.
773 Paleoceanography and Paleoclimatology 35, 22.10.1029/2019pa003785.

774 Macalady, J.L., Vestling, M.M., Baumler, D., Boekelheide, N., Kaspar, C.W. and Banfield, J.F.
775 (2004) Tetraether-linked membrane monolayers in Ferroplasma spp: a key to survival in acid.
776 Extremophiles 8, 411-419.10.1007/s00792-004-0404-5.

777 Martin, C., Menot, G., Thouveny, N., Peyron, O., Andrieu-Ponel, V., Montade, V., Davtian, N.,
778 Reille, M. and Bard, E. (2020) Early Holocene Thermal Maximum recorded by branched
779 tetraethers and pollen in Western Europe (Massif Central, France). Quaternary Science Reviews
780 228, 21.10.1016/j.quascirev.2019.106109.

781 Martinez-Sosa, P. and Tierney, J.E. (2019) Lacustrine brGDGT response to microcosm and
782 mesocosm incubations. Organic Geochemistry 127, 12-22.10.1016/j.orggeochem.2018.10.011.

783 Martinez-Sosa, P., Tierney, J.E., Stefanescu, I.C., Crampton-Flood, E.D., Shuman, B.N. and
784 Routson, C. (2021) A global Bayesian temperature calibration for lacustrine brGDGTs.
785 Geochimica Et Cosmochimica Acta 305, 87-105.10.1016/j.gca.2021.04.038.

786 Mensing, S.A., Sharpe, S.E., Tunno, I., Sada, D.W., Thomas, J.M., Starratt, S. and Smith, J.
787 (2013) The Late Holocene Dry Period: multiproxy evidence for an extended drought between
788 2800 and 1850 cal yr BP across the central Great Basin, USA. Quaternary Science Reviews 78,
789 266-282.10.1016/j.quascirev.2013.08.010.

790 Millar, C.I., Charlet, D.A., Delany, D.L., King, J.C. and Westfall, R.D. (2019) Shifts of
791 demography and growth in limber pine forests of the Great Basin, USA, across 4000 yr of
792 climate variability. Quaternary Research 91, 691-704.10.1017/qua.2018.120.

793 Moser, K.A. and Kimball, J.P. (2009) A 19,000-year record of hydrologic and climatic change
794 inferred from diatoms from Bear Lake, Utah and Idaho, Paleoenvironments of Bear Lake, Utah
795 and Idaho, and Its Catchment. Geological Soc Amer Inc, Boulder, pp. 229-246.

796 Naeher, S., Niemann, H., Peterse, F., Smittenberg, R.H., Zigah, P.K. and Schubert, C.J. (2014)
797 Tracing the methane cycle with lipid biomarkers in Lake Rotsee (Switzerland). Organic
798 Geochemistry 66, 174-181.10.1016/j.orggeochem.2013.11.002.

799 Naftz, D. (2017) Inputs and Internal Cycling of Nitrogen to a Causeway Influenced, Hypersaline
800 Lake, Great Salt Lake, Utah, USA. Aquatic Geochemistry 23, 199-216.10.1007/s10498-017-
801 9318-6.

802 Natalicchio, M., Birgel, D., Peckmann, J., Lozar, F., Carnevale, G., Liu, X.L., Hinrichs, K.U. and
803 Dela Pierre, F. (2017) An archaeal biomarker record of paleoenvironmental change across the
804 onset of the Messinian salinity crisis in the absence of evaporites (Piedmont Basin, Italy).
805 Organic Geochemistry 113, 242-253.10.1016/j.orggeochem.2017.08.014.

806 National Centers for Environmental Information (2022) Time series- monthly GHCN v3 mean
807 temperature- Salt Lake Cit (United States of America),

808 Null, S.E. and Wurtsbaugh, W.A. (2020) Water Development, Consumptive Water Uses, and the
809 Great Salt Lake, in: Baxter, B.K., Butler, J.K. (Eds.), Great Salt Lake Biology, A Terminal Lake
810 in a Time of Change. Springer Nature Switzerland AG, Cham, Switzerland, pp. 1-21.

811 Oviatt, C.G., Atwood, G. and Thompson, R.S. (2021) History of Great Salt Lake, Utah, USA:
812 since the Termination of Lake Bonneville, in: Rosen, M.R., Finkelstein, D.B., Park Boush, L.,
813 Pla-Pueyo, S. (Eds.), Limnogeology: Progress, Challenges and Opportunities : A Tribute to
814 Elizabeth Gierlowski-Kordesch. Springer International Publishing, Cham, pp. 233-271.

815 Peaple, M.D., Bhattacharya, T., Lowenstein, T.K., McGee, D., Olson, K.J., Stroup, J.S., Tierney,
816 J.E. and Feakins, S.J. (2022) Biomarker and Pollen Evidence for Late Pleistocene Pluvials in the
817 Mojave Desert. Paleoceanography and Paleoclimatology 37, 20.10.1029/2022pa004471.

818 Peaple, M.D., Tierney, J.E., McGee, D., Lowenstein, T.K., Bhattacharya, T. and Feakins, S.J.
819 (2021) Identifying plant wax inputs in lake sediments using machine learning. Organic
820 Geochemistry 156, 11.10.1016/j.orggeochem.2021.104222.

Peltier, W.R., Argus, D.F. and Drummond, R. (2015) Space geodesy constrains ice age terminal deglaciation: The global ICE-6G_C (VM5a) model. Journal of Geophysical Research-Solid Earth 120, 450-487.10.1002/2014jb011176.

Perry, K.D., Crosman, E.T. and Hoch, S.W. (2019) Results of the Great Salt Lake Dust Plume Study (2016-2018). University of Utah, Salt Lake City, UT, USA

Peterse, F., van der Meer, J., Schouten, S., Weijers, J.W.H., Fierer, N., Jackson, R.B., Kim, J.H. and Damste, J.S.S. (2012) Revised calibration of the MBT-CBT paleotemperature proxy based on branched tetraether membrane lipids in surface soils. Geochimica Et Cosmochimica Acta 96, 215-229.10.1016/j.gca.2012.08.011.

Raberg, J.H., Harning, D.J., Crump, S.E., de Wet, G., Blumm, A., Kopf, S., Geirsdottir, A., Miller, G.H. and Sepulveda, J. (2021) Revised fractional abundances and warm-season temperatures substantially improve brGDGT calibrations in lake sediments. Biogeosciences 18, 3579-3603.10.5194/bg-18-3579-2021.

Raberg, J.H., Miller, G.H., Geirsdottir, A. and Sepulveda, J. (2022) Near-universal trends in brGDGT lipid distributions in nature. Science Advances 8, 12.10.1126/sciadv.abm7625.

Ramirez, R. (2022) Great Salt Lake is 'in trouble' as level falls to lowest on record for second year in a row. CNN

Ramos-Roman, M.J., De Jonge, C., Magyari, E., Veres, D., Ilvonen, L., Develle, A.L. and Seppa, H. (2022) Lipid biomarker (brGDGT)- and pollen-based reconstruction of temperature change during the Middle to Late Holocene transition in the Carpathians. Global and Planetary Change 215, 13.10.1016/j.gloplacha.2022.103859.

Routson, C.C., Erb, M.P. and McKay, N.P. (2022) High Latitude Modulation of the Holocene North American Monsoon. Geophysical Research Letters 49, 10.10.1029/2022gl099772.

Rupke, A. and McDonald, A. (2012) Great Salt Lake brine chemistry database, 1966-2011, Utah Geological Survey Open-File Report. Utah Geological Survey, Salt Lake City Utah, p. 7.10.34191/OFR-596.

847 Russell, J.M., Hopmans, E.C., Loomis, S.E., Liang, J. and Damste, J.S.S. (2018) Distributions of
848 5-and 6-methyl branched glycerol dialkyl glycerol tetraethers (brGDGTs) in East African lake
849 sediment: Effects of temperature, pH, and new lacustrine paleotemperature calibrations. Organic
850 Geochemistry 117, 56-69.10.1016/j.orggeochem.2017.12.003.

851 Schouten, S., Hopmans, E.C. and Damste, J.S.S. (2013) The organic geochemistry of glycerol
852 dialkyl glycerol tetraether lipids: A review. Organic Geochemistry 54, 19-
853 61.10.1016/j.orggeochem.2012.09.006.

854 Shin, S.I., Sardeshmukh, P.D., Webb, R.S., Oglesby, R.J. and Barsugli, J.J. (2006)
855 Understanding the mid-Holocene climate. Journal of Climate 19, 2801-2817.10.1175/jcli3733.1.

856 Shope, C.L. and Angeroth, C.E. (2015) Calculating salt loads to Great Salt Lake and the
857 associated uncertainties for water year 2013; updating a 48 year old standard. Science of the
858 Total Environment 536, 391-405.10.1016/j.scitotenv.2015.07.015.

859 Shuman, B., Bartlein, P., Logar, N., Newby, P. and Webb, T. (2002) Parallel climate and
860 vegetation responses to the early Holocene collapse of the Laurentide Ice Sheet. Quaternary
861 Science Reviews 21, 1793-1805.10.1016/s0277-3791(02)00025-2.

862 Shuman, B., Huang, Y.S., Newby, P. and Wang, Y. (2006) Compound-specific isotopic analyses
863 track changes in seasonal precipitation regimes in the Northeastern United States at ca 8200cal
864 yrBP. Quaternary Science Reviews 25, 2992-3002.10.1016/j.quascirev.2006.02.021.

865 Shuman, B.N. and Marsicek, J. (2016) The structure of Holocene climate change in mid-latitude
866 North America. Quaternary Science Reviews 141, 38-51.10.1016/j.quascirev.2016.03.009.

867 Shuman, B.N. and Serravezza, M. (2017) Patterns of hydroclimatic change in the Rocky
868 Mountains and surrounding regions since the last glacial maximum. Quaternary Science Reviews
869 173, 58-77.10.1016/j.quascirev.2017.08.012.

870 So, R., Lowenstein, T., Jagniecki, E., Tierney, J.E. and Feakins, S.J. (2022) NOAA/WDS
871 Paleoclimatology - Great Salt Lake, Utah Biomarker Data from the Holocene [Dataset], NOAA
872 National Centers for Environmental Information. https://doi.org/10.25921/f3hg-4e71.

873 Sorensen, E.D., Hoven, H.M. and Neill, J. (2020) Great Salt Lake Shorebirds, Their Habitats,
874 and Food Base, in: Baxter, B.K., Butler, J.K. (Eds.), Great Salt Lake Biology, A Terminal Lake
875 in a Time of Change. Springer Nature Switzerland AG, Cham, Switzerland, pp. 263-309.

876 Stefanescu, I.C., Shuman, B.N. and Tierney, J.E. (2021) Temperature and water depth effects on
877 brGDGT distributions in sub-alpine lakes of mid-latitude North America. Organic Geochemistry
878 152, 15.10.1016/j.orggeochem.2020.104174.

879 Steponaitis, E., Andrews, A., McGee, D., Quade, J., Hsieh, Y.T., Broecker, W.S., Shuman, B.N.,
880 Burns, S.J. and Cheng, H. (2015) Mid-Holocene drying of the US Great Basin recorded in
881 Nevada speleothems. Quaternary Science Reviews 127, 174-
882 185.10.1016/j.quascirev.2015.04.011.

883 Stine, S. (1990) Late Holocene fluctuations of Mono Lake, eastern California. Palaeogeography
884 Palaeoclimatology Palaeoecology 78, 333-&.10.1016/0031-0182(90)90221-r.

885 Teixidor, P., Grimalt, J.O., Pueyo, J.J. and Rodriguezvalera, F. (1993) Isopranylglycerol diethers
886 in nonalkaline evaporitic environments. Geochimica Et Cosmochimica Acta 57, 4479-
887 4489.10.1016/0016-7037(93)90497-k.

888 Thompson, A.J., Zhu, J., Poulsen, C.J., Tierney, J.E. and Skinner, C.B. (2022) Northern
889 Hemisphere vegetation change drives a Holocene thermal maximum. Science Advances 8,
890 10.10.1126/sciadv.abj6535.

891 Turich, C. and Freeman, K.H. (2011) Archaeal lipids record paleosalinity in hypersaline systems.
892 Organic Geochemistry 42, 1147-1157.10.1016/j.orggeochem.2011.06.002.

893 United States Geological Survey (2022a) Bear River near Corinne, UT (10126000), National
894 Water Dashboard

895 United States Geological Survey (2022b) Great Salt Lake at Saltair Harbor, UT (10010000),
896 National Water Dashboard

897 Vandier, F., Tourte, M., Doumbe-Kingue, C., Plancq, J., Schaeffer, P., Oger, P. and Grossi, V.
898 (2021) Reappraisal of archaeal C-20-C-25 diether lipid (extended archaeol) origin and use as a
899 biomarker of hypersalinity. Organic Geochemistry 159, 5.10.1016/j.orggeochem.2021.104276.

900 Wang, H.Y., Liu, W.G., He, Y.X., Zhou, A.F., Zhao, H., Liu, H., Cao, Y.N., Hu, J., Meng, B.W.,
901 Jiang, J.W., Kolpakova, M., Krivonogov, S. and Liu, Z.H. (2021) Salinity-controlled
902 isomerization of lacustrine brGDGTs impacts the associated MBT5ME terrestrial temperature
903 index. Geochimica Et Cosmochimica Acta 305, 33-48.10.1016/j.gca.2021.05.004.

904 Weijers, J.W.H., Schouten, S., van den Donker, J.C., Hopmans, E.C. and Damste, J.S.S. (2007)
905 Environmental controls on bacterial tetraether membrane lipid distribution in soils. Geochimica
906 Et Cosmochimica Acta 71, 703-713.10.1016/j.gca.2006.10.003.

907 Wurtsbaugh, W.A., Miller, C., Null, S.E., DeRose, R.J., Wilcock, P., Hahnenberger, M., Howe,
908 F. and Moore, J. (2017) Decline of the world's saline lakes. Nature Geoscience 10, 816-
909 +.10.1038/ngeo3052.

910 Xiao, W.J., Wang, Y.H., Zhou, S.Z., Hu, L.M., Yang, H. and Xu, Y.P. (2016) Ubiquitous
911 production of branched glycerol dialkyl glycerol tetraethers (brGDGTs) in global marine
912 environments: a new source indicator for brGDGTs. Biogeosciences 13, 5883-5894.10.5194/bg-
913 13-5883-2016.
914

Figure 1.

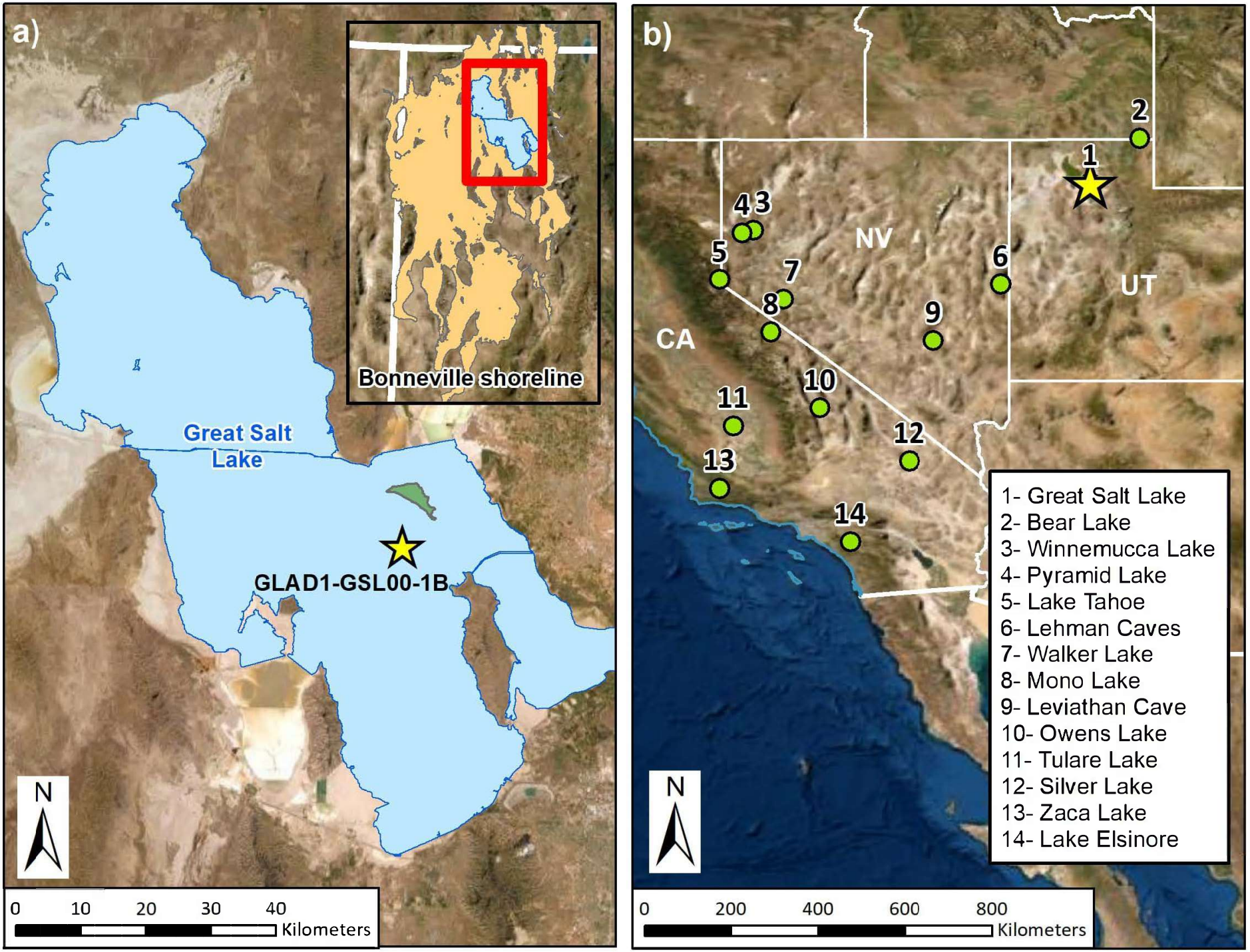
a)
Bonneville shoreline
Great Salt Lake
GLAD1-GSL00-1B
N
0 10 20 30 40
Kilometers
b)
NV
UT
CA
1
2
3
4
5
6
7
8
9
10
11
12
13
14
1- Great Salt Lake
2- Bear Lake
3- Winnemucca Lake
4- Pyramid Lake
5- Lake Tahoe
6- Lehman Caves
7- Walker Lake
8- Mono Lake
9- Leviathan Cave
10- Owens Lake
11- Tulare Lake
12- Silver Lake
13- Zaca Lake
14- Lake Elsinore
N
0 200 400 600 800
Kilometers

Figure 2.

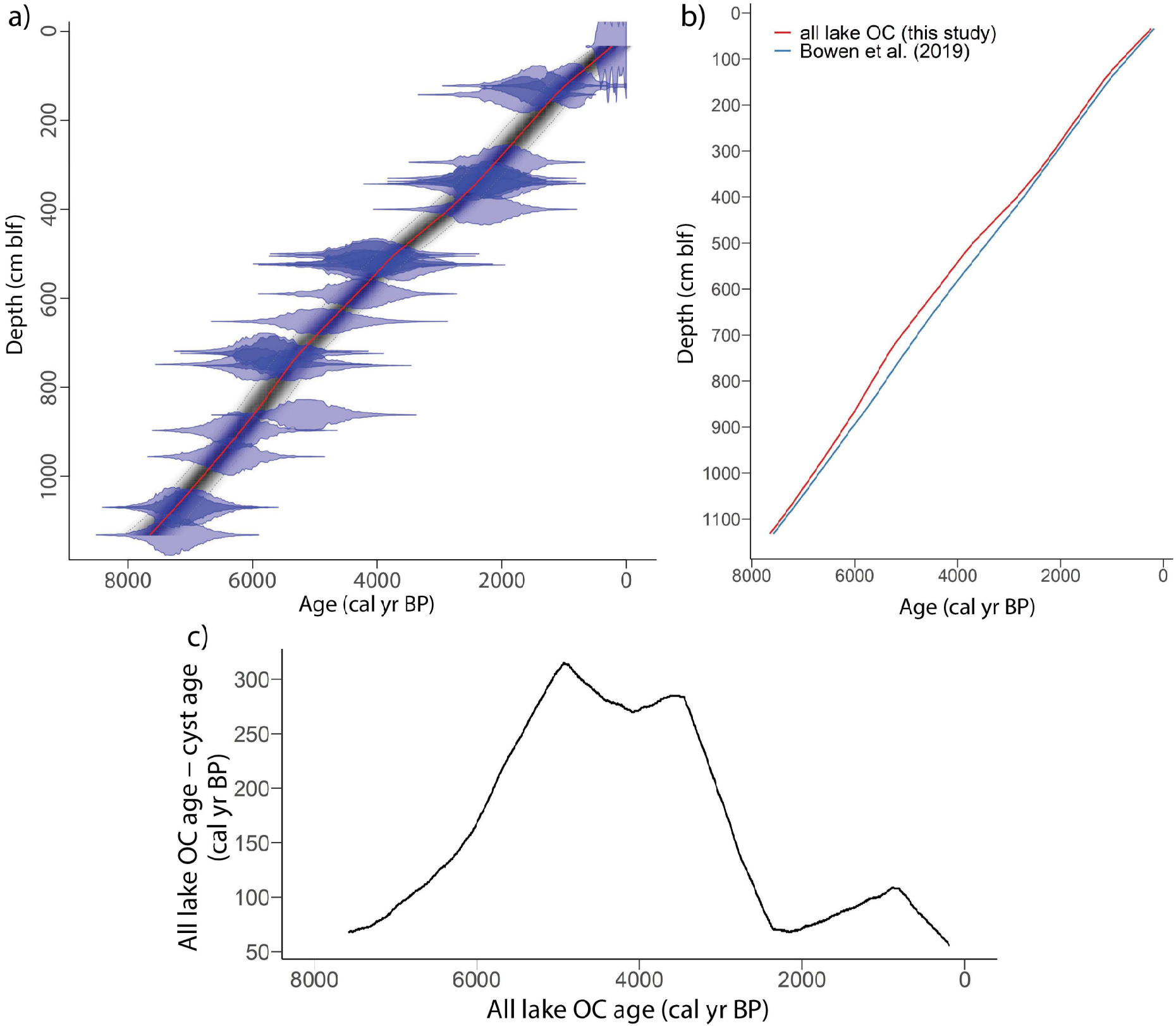
a)
Depth (cm blf)
0
200
400
600
800
1000
8000
6000
4000
2000
0
Age (cal yr BP)
b)
all lake OC (this study)
Bowen et al. (2019)
Depth (cm blf)
0
100
200
300
400
500
600
700
800
900
1000
1100
8000
6000
4000
2000
0
Age (cal yr BP)
c)
All lake OC age – cyst age (cal yr BP)
300
250
200
150
100
50
8000
6000
4000
2000
0
All lake OC age (cal yr BP)

Figure 3.

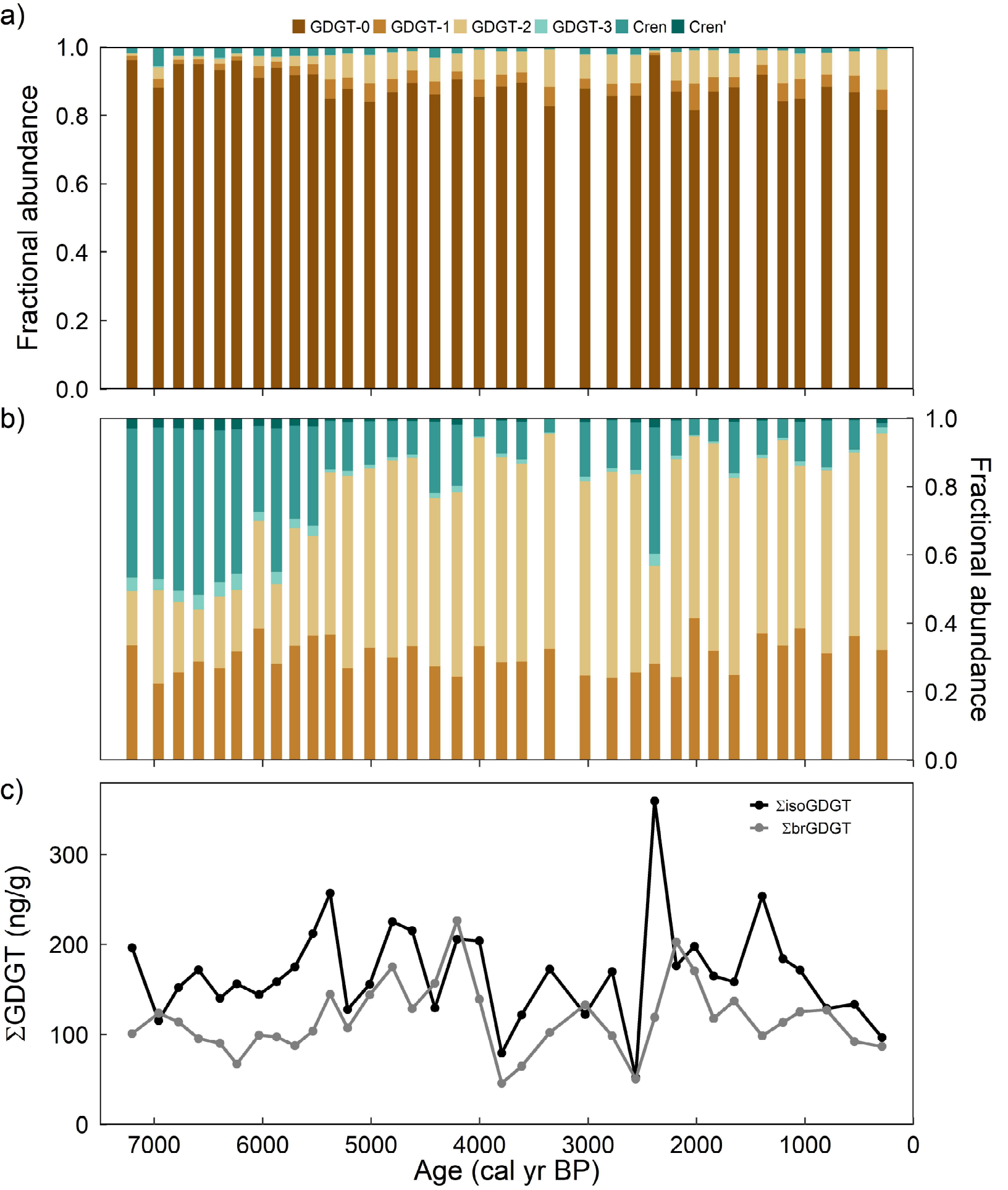
a)
GDGT-0
GDGT-1
GDGT-2
GDGT-3
Cren
Cren'
Fractional abundance
1.0
0.8
0.6
0.4
0.2
0.0
b)
Fractional abundance
1.0
0.8
0.6
0.4
0.2
0.0
c)
ΣisoGDGT
ΣbrGDGT
ΣGDGT (ng/g)
300
200
100
0
7000
6000
5000
4000
3000
2000
1000
0
Age (cal yr BP)

Figure 4.

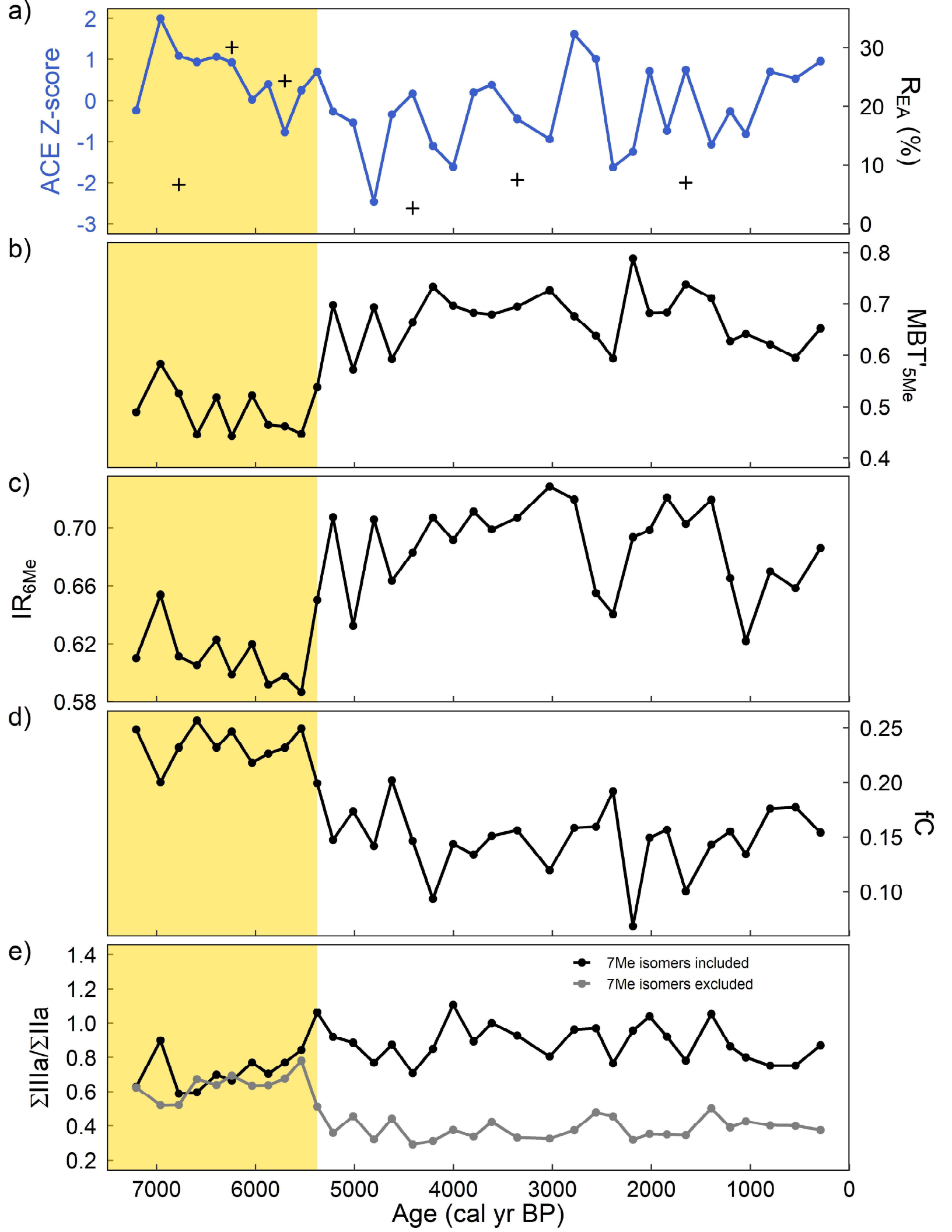
a)
ACE Z-score
2
1
0
-1
-2
-3
R_{EA} (%)
30
20
10
0
b)
MBT'_{5Me}
0.8
0.7
0.6
0.5
0.4
c)
IR_{6Me}
0.70
0.66
0.62
0.58
d)
fC
0.25
0.20
0.15
0.10
e)
$\Sigma IIIa/\Sigma IIa$
1.4
1.2
1.0
0.8
0.6
0.4
0.2
7Me isomers included
7Me isomers excluded
7000
6000
5000
4000
3000
2000
1000
0
Age (cal yr BP)

Figure 5.

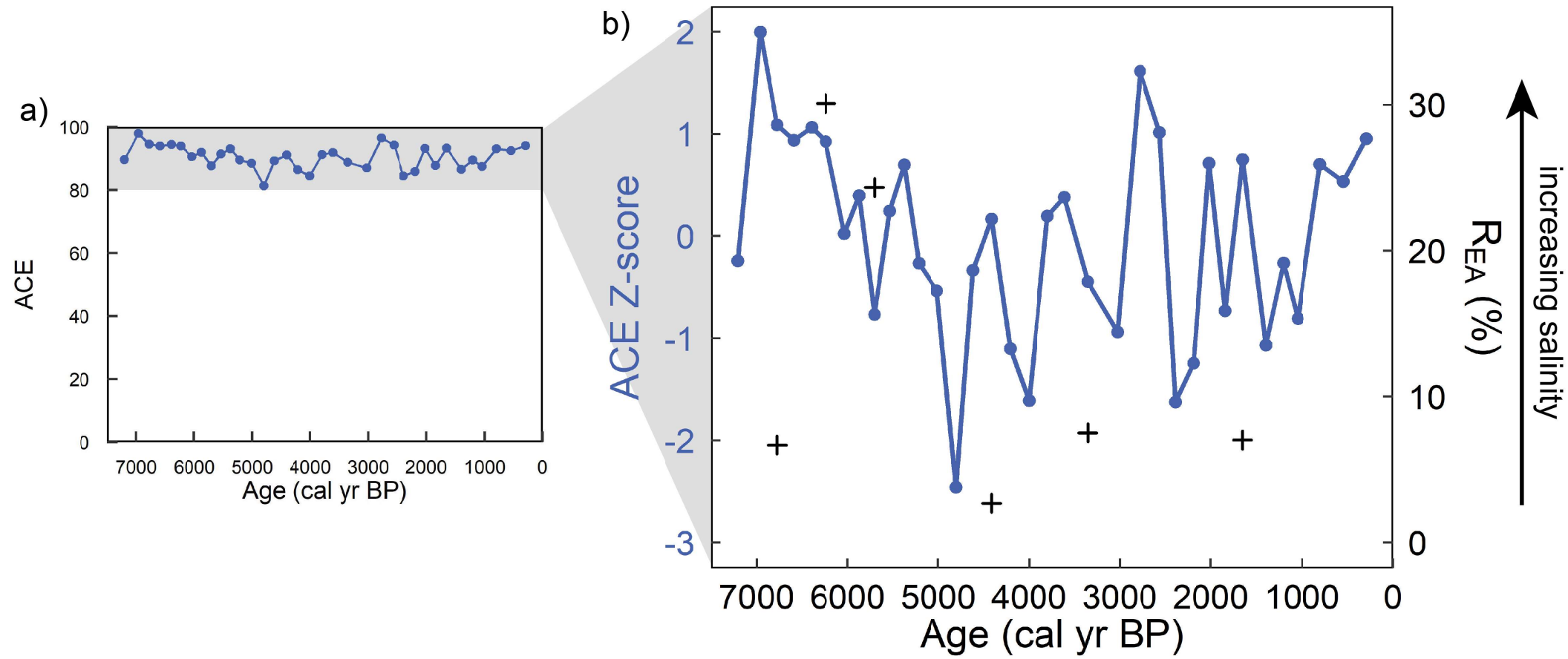
a)
ACE
100
80
60
40
20
0
7000 6000 5000 4000 3000 2000 1000 0
Age (cal yr BP)
b)
ACE Z-score
2
1
0
-1
-2
-3
30
20
10
0
R_{EA} (%)
increasing salinity
7000 6000 5000 4000 3000 2000 1000 0
Age (cal yr BP)

Figure 6.

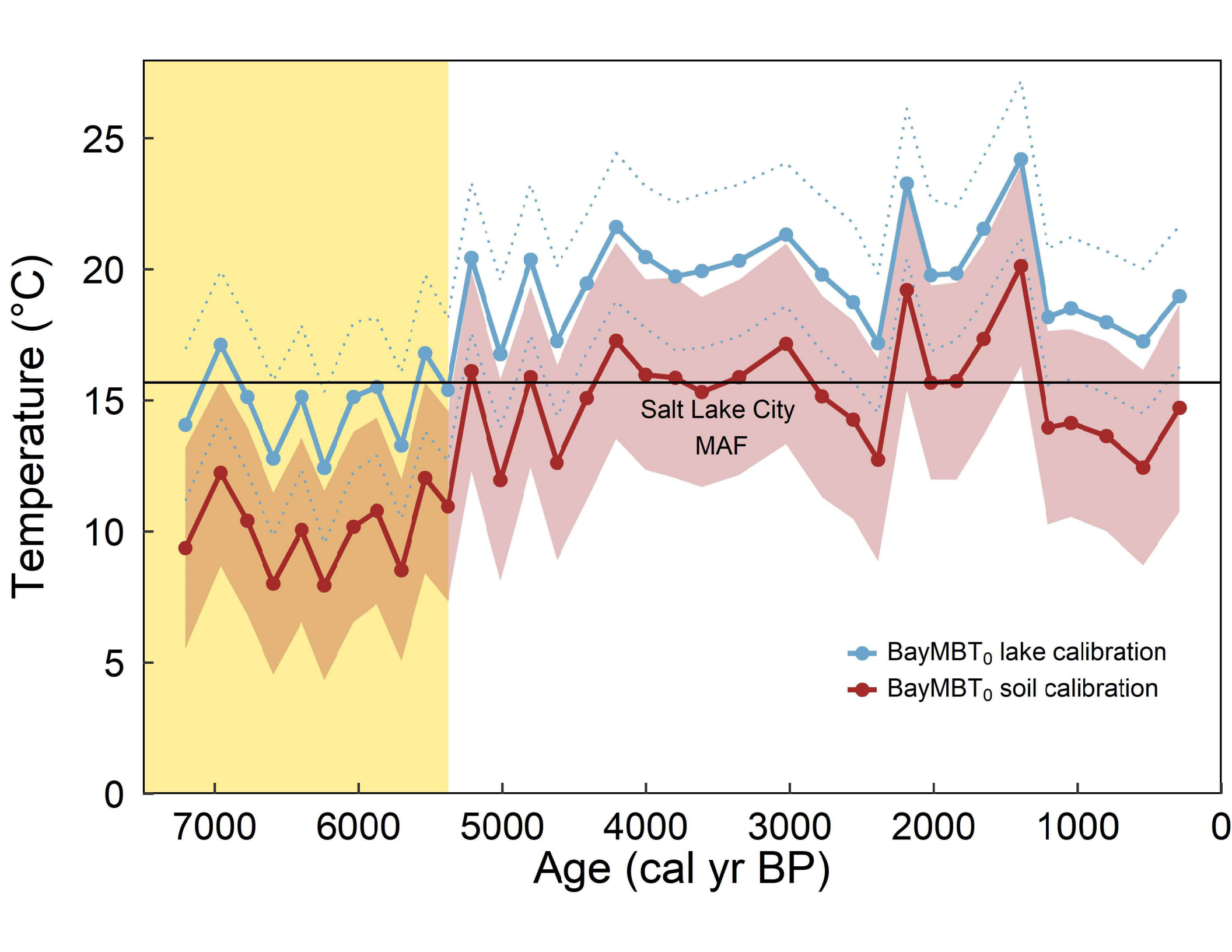
Temperature (°C)
25
20
15
10
5
0
7000
6000
5000
4000
3000
2000
1000
0
Age (cal yr BP)
Salt Lake City
MAF
BayMBT0 lake calibration
BayMBT0 soil calibration

Figure 7.

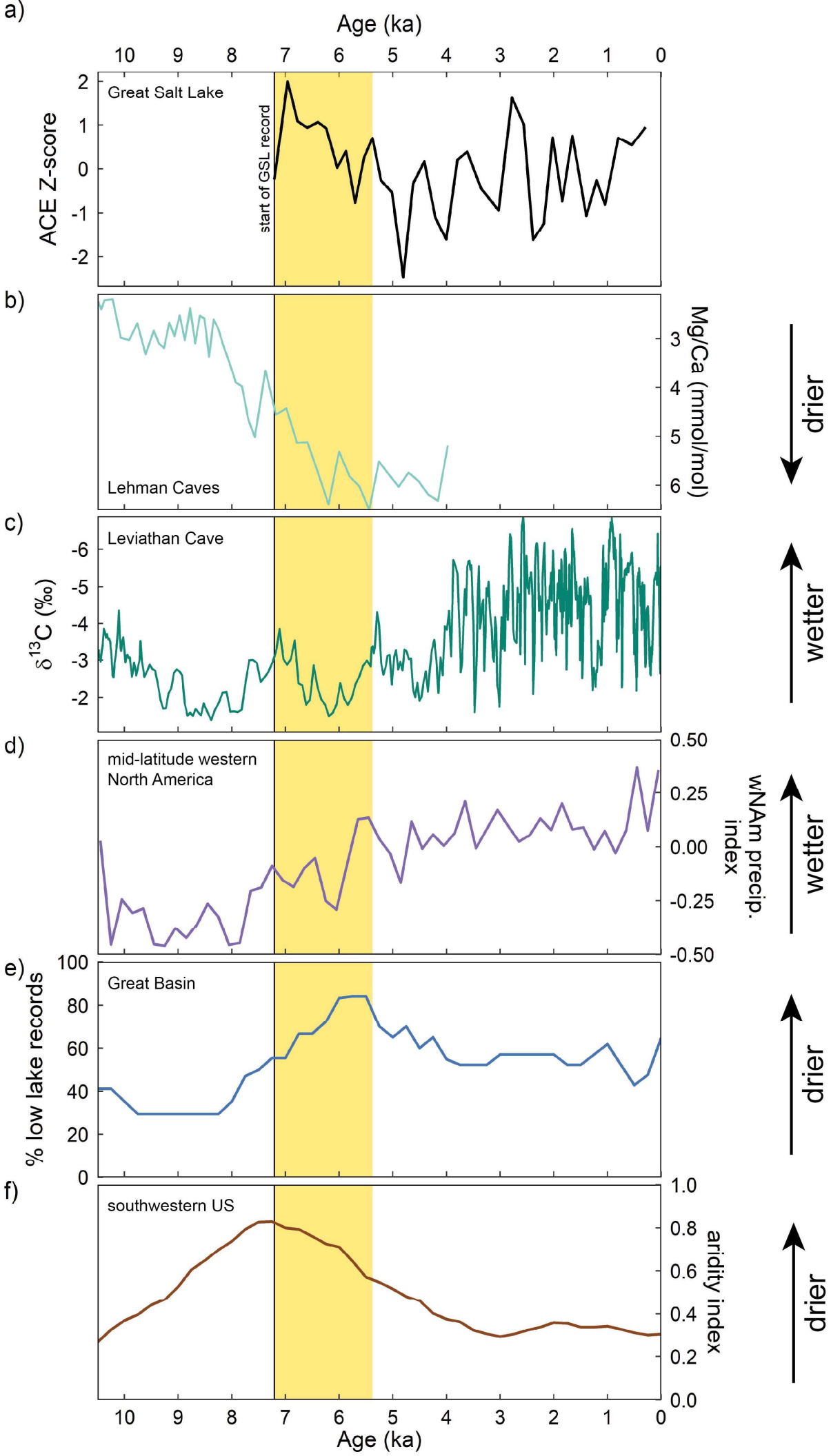
a)
Age (ka)
10 9 8 7 6 5 4 3 2 1 0
Great Salt Lake
start of GSL record
ACE Z-score
2 1 0 -1 -2
b)
Lehman Caves
Mg/Ca (mmol/mol)
3 4 5 6
drier
c)
Leviathan Cave
δ13C (‰)
-6 -5 -4 -3 -2
wetter
d)
mid-latitude western North America
wNAm precip. index
0.50 0.25 0.00 -0.25 -0.50
wetter
e)
Great Basin
% low lake records
100 80 60 40 20 0
drier
f)
southwestern US
aridity index
1.0 0.8 0.6 0.4 0.2 0.0
drier
Age (ka)
10 9 8 7 6 5 4 3 2 1 0

Paleoceanography and Paleoclimate

Supporting Information for

Holocene water balance variations in Great Salt Lake, Utah: application of GDGT indices and the ACE salinity proxy

Rachel T. So[1*], Tim K. Lowenstein[2], Elliot Jagniecki[3], Jessica E. Tierney[4], Sarah J. Feakins[1]

[1]Department of Earth Sciences, University of Southern California, Los Angeles, CA 90089, USA.
[2]Department of Geological Sciences and Environmental Studies, Binghamton University, Binghamton, NY 13902, USA.
[3]Utah Geological Survey, Salt Lake City, UT 84114, USA.
[4]Department of Geoscience, University of Arizona, Tucson, AZ 85721, USA.
*Correspondence to: Rachel T. So rtso@usc.edu

Contents of this file

Figures S1 to S6

Introduction

The supporting information associated with the manuscript referenced above includes six supplementary figures. Figure S1 is an example chromatogram of a GSL sample from this study. Figure S2 shows changepoint analysis for detecting changes in the mean and variance of select GDGT indices calculated for this study's GSL samples. Figure S3 is a compilation of all GDGT indices calculated for this study's GSL samples. Figure S4 shows principal component analyses using brGDGT distributions of GSL samples, compared to global lakes and soils. Figure S5 shows the brGDGT distributions of lake sediment and soils compared against GSL sediments. Figure S6 is a ternary diagram of tetra-, penta-, and hexamethyl brGDGT proportions in GSL samples compared to global lakes and soils.

Supplementary Figures

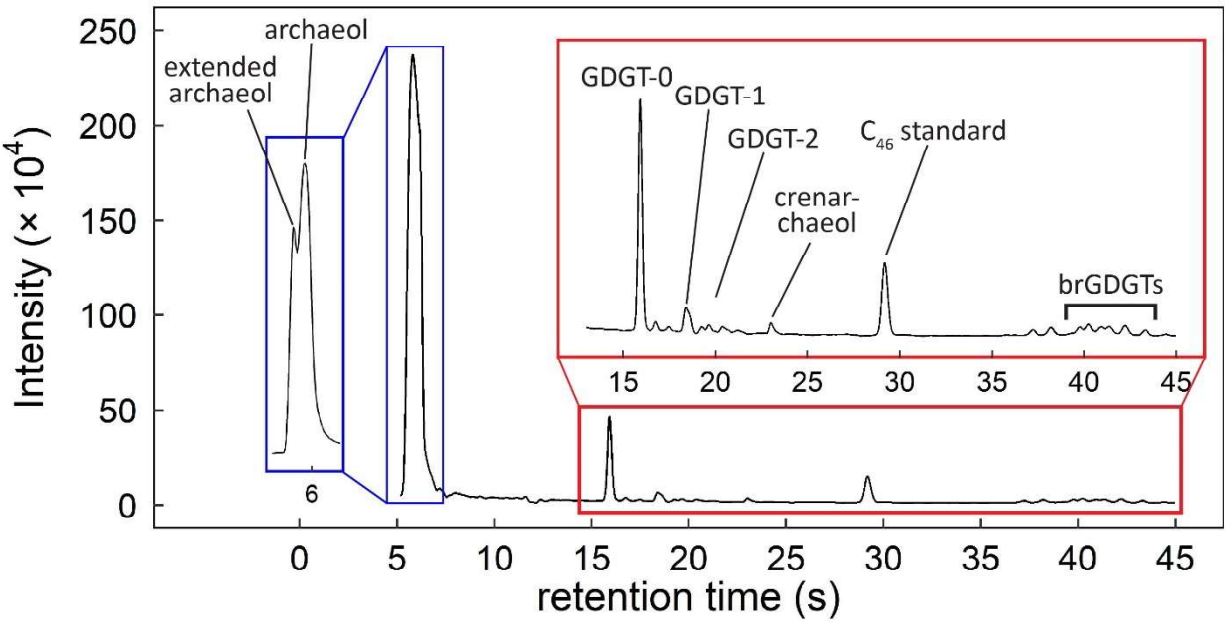

Figure S1. An example chromatogram representative of GSL samples from this study (GLAD1-GSL00-1B, 906-907cm). Labeled in the chromatogram are the individual peaks of archaeol, extended archaeol, GDGT-0, GDGT-1, GDGT-2, crenarchaeol, and the C_{46} standard along with the region containing brGDGTs.

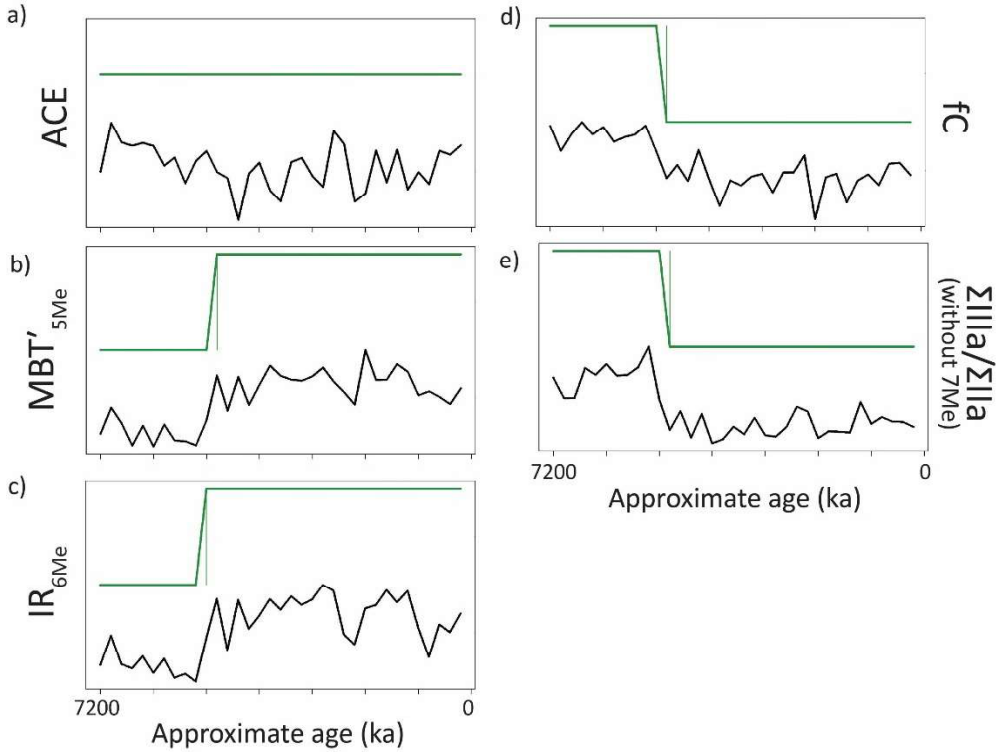

Figure S2. Environmental time series changepoint detection using the R package EnvCpt applied to a) ACE, b) MBT'_{5Me}, c) IR_{6Me}, d) fC, and e) ΣIIIa/ΣIIa without 7-methyl isomers. The method used identifies changepoints in the series mean and variance.

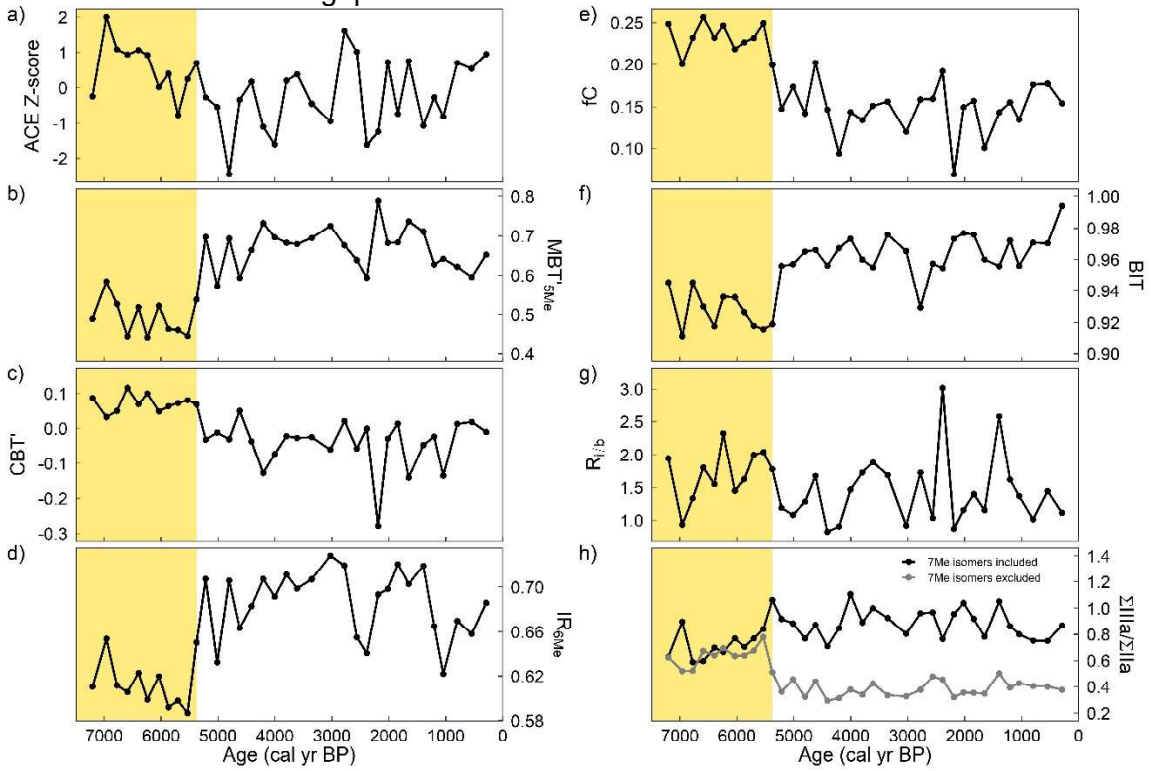

Figure S3. Temporal variations in GDGT indices showing a) ACE Z-scores, b) MBT'_{5Me}, c) CBT', d) IR_{6Me}, e) fC, f) BIT, g) $R_{i/b}$, and h) ΣIIIa/ΣIIa. Yellow shading indicates the portion of the record prior to the step change seen in four indices (MBT'_{5Me}, IR_{6Me}, fC, and ΣIIIa/ΣIIa).

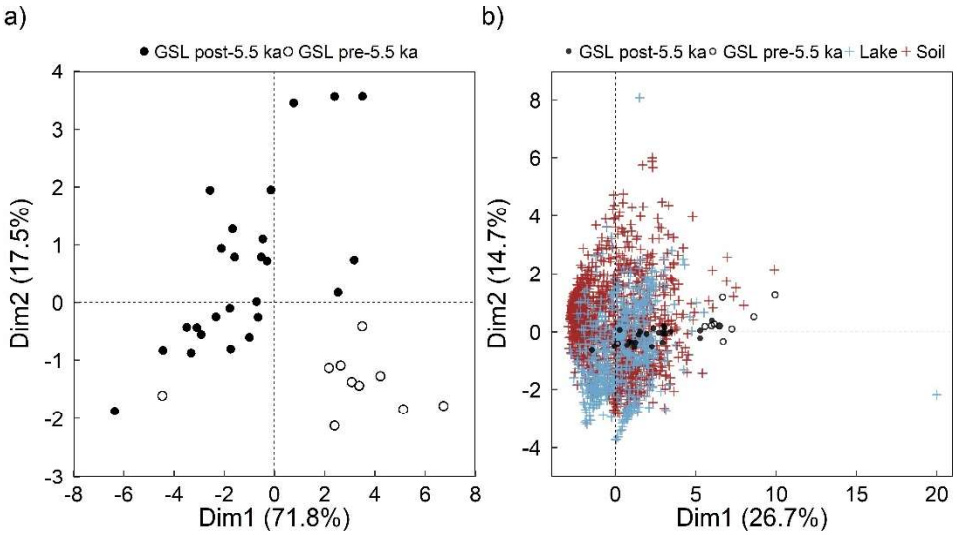

Figure S4. Principal component analyses (PCA) using brGDGT distributions of a) pre- (open circle) and post-5.5 ka (filled circle) GSL sediments, and b) compared to global lakes (blue cross) and soils (red cross) compilation of Raberg et al. (2022).

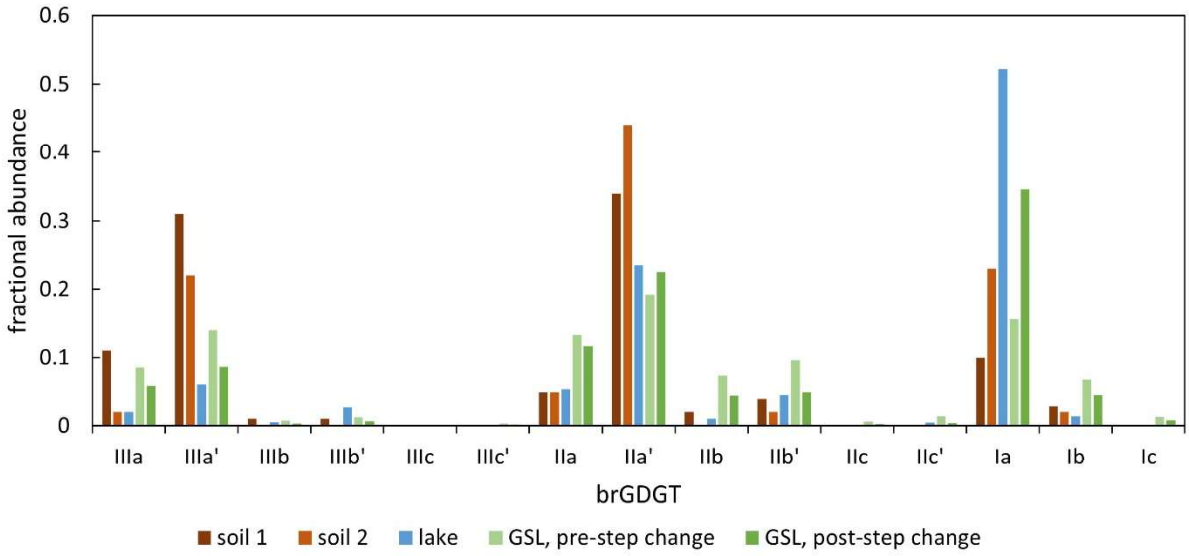

Figure S5. BrGDGT distribution of GSL samples from before and after the 5.5 ka step shift, and comparison to soils and lake distributions from southwestern US sites. Comparison brGDGT distributions were obtained from the soil compilation of Dearing Crampton-Flood et al. (2020), and lake compilation of Martinez-Sosa et al. (2021), showing Mono Lake (CA).

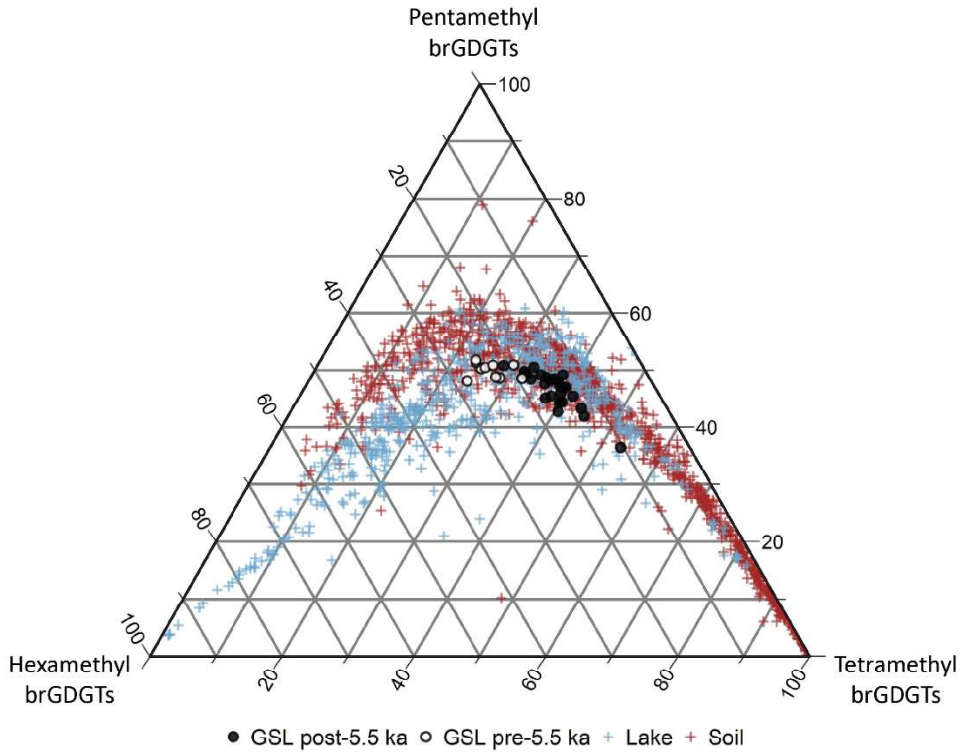

Figure S6. Ternary diagram showing the proportions of tetra-, penta-, and hexamethyl brGDGTs (I, II, and III respectively) in GSL sediments, differentiated into pre-5.5 ka (white circle) and post 5.5 ka (black circle), and the global lakes (blue cross) and soils (red cross) compilation of Raberg et al. (2022).